FGF signaling in development beyond canonical pathways

Ayan T. Ray, Pierre Mazot[1], J. Richard Brewer[2], Catarina Catela[3], Colin J. Dinsmore, and Philippe Soriano*

Department of Cell, Developmental, and Regenerative Biology
Icahn School of Medicine at Mount Sinai
New York, NY 10029

*Corresponding author: philippe.soriano@mssm.edu

Present address: [1]INSERM Transfert, Paris, France
[2]Department of Immunobiology, Yale University, New Haven, CT 06520
[3]Department of Neurobiology, University of Chicago, Chicago, IL 60637

Keywords: FGF; ERK1/2; Craniofacial development; Neural crest; Cell adhesion

FGFs are key developmental regulators which engage a signal transduction cascade through receptor tyrosine kinases, typically involving ERK1/2, PI3K/AKT, and other effectors. However, it remains unknown if all FGF activities depend on kinase activity or these canonical signal transduction cascades. To address these questions, we generated allelic series of knock-in *Fgfr1* and *Fgfr2* mouse strains, carrying point mutations that disrupt binding of signaling effectors to the receptors, alone or in combination. We also produced a kinase dead allele of *Fgfr2* which broadly phenocopies the null mutant. When interrogated in cranial neural crest cells, point mutations in either receptor revealed discrete functions for signaling pathways in specific craniofacial contexts, but failed to recapitulate the single or double null mutant phenotypes even in their most extensive combination. Furthermore, we found that together these signaling mutations abrogated the established FGF-induced signal transduction pathways, yet certain FGF functions such as cell-matrix and cell-cell adhesion remained unaffected. Our studies establish combinatorial roles of both *Fgfr1* and *Fgfr2* in development and identify novel kinase-dependent cell adhesion properties of FGF receptors, independent of well-established roles in intracellular signaling.

Classic models of receptor tyrosine kinase activation involve ligand binding, receptor dimerization, transactivation of the kinase domain, phosphorylation of intracellular tyrosines, and binding of effectors that orchestrate activation of downstream signaling pathways [1]. Different thresholds in dimer strength and stability may also come into play to regulate signaling dynamics [2-4]. For FGFRs, where downstream pathways have been particularly well studied, numerous lines of evidence point to ERK1/2 as the main effector of FGF signaling [5,6]. Although characterization of effector binding to RTKs provides critical insights on signaling specificity, assessing relative pathway significance requires *in vivo* validation. A previous analysis showed that knock-in *Fgfr1* point mutations disrupting binding of multiple signaling effectors, alone or in combination, did not recapitulate the *Fgfr1*$^{-/-}$ phenotype despite eliminating ERK1/2 outputs [7]. These results, although suggestive of additional signaling pathways, were difficult to interpret due to expression of another receptor, FGFR2. Using cranial neural crest (cNCC)-derived mesenchyme to understand FGF signaling, we now investigate the relative contributions of both FGF receptors and their signaling outputs to craniofacial development. We find that signaling mutations for each receptor disrupt classical signal transduction pathways in the absence of the other receptor, but do not recapitulate the null phenotypes. We furthermore show that FGF signaling is kinase-dependent and identify non-canonical functions of FGF signaling that help reconcile the gap in our phenotypic analyses.

69

70 ## *Fgfr1* and *Fgfr2* orchestrate craniofacial development by regulating cell survival

71 To interrogate FGFR1/2 functions, we initially investigated how loss of both receptors in cNCCs
72 influences craniofacial development. We found both receptors extensively co-expressed in the
73 cNCC-derived mesenchyme and overlying epithelia, using fluorescent *Fgfr1* and *Fgfr2* reporter
74 alleles (Extended Data Fig. 1A). Next, conditional null alleles (henceforth denoted *cKO*) of *Fgfr1*
75 and *Fgfr2* were combined with *Wnt1Cre* drivers active in NCCs [8,9]. At embryonic day (E) 18.5,
76 *Fgfr1*$^{cKO/cKO}$ embryos displayed a fully penetrant facial cleft, *Fgfr2*$^{cKO/cKO}$ mutants had no overt
77 phenotype, and *Fgfr1*$^{cKO/cKO}$; *Fgfr2*$^{cKO/cKO}$ double mutants exhibited severe agenesis of most NCC
78 derived craniofacial structures including the frontal and nasal bones, nasal cartilage, maxilla, and
79 mandible (Fig. 1A and Extended Data Fig. 1B). Both *Fgfr1*$^{cKO/cKO}$; *Fgfr2*$^{cKO/+}$ and *Fgfr1*$^{cKO/cKO}$;
80 *Fgfr2*$^{cKO/cKO}$ embryos exhibited defects in mandible development with hypomorphic proximal
81 structures including angular and coronoid processes (Extended Data Fig. 1C). Overall, double
82 mutants showed reduced or no ossification of cNCC-derived craniofacial skeletal structures
83 (Extended Data Fig. 1B-D and Supplementary Information Fig. S1A-D). At E9.5 and E10.5,
84 *Fgfr1*$^{cKO/cKO}$; *Fgfr2*$^{cKO/cKO}$; *ROSA26*$^{mT/mG}$ double mutants developed hypoplastic pharyngeal arches
85 with reduced NCC lineage GFP^{+} cells (Fig. 1B and Extended Data Fig. 2A). We observed reduced
86 expression of facial prominence markers along with midline morphogenesis defects, but ectoderm
87 gene expression remained unaffected, suggesting reduced NCC numbers rather than patterning
88 defects (Extended Data Fig. 2B). FGFR1 and FGFR2 are thought to function predominantly in
89 mesenchymal or epithelial contexts, respectively, since *Fgfr1c* mutants recapitulate many aspects
90 of the *Fgfr1*$^{-/-}$ phenotype [10], and *Fgfr2b* mutants are reminiscent of *Fgfr2*$^{-/-}$ embryos [11]. Here, we
91 show that both receptors function coordinately within the NCC-derived mesenchyme, as
92 combined loss of *Fgfr1* and *Fgfr2* leads to significantly more severe midface and mandibular
93 defects than loss of either receptor alone.

94 A reduction in NCC numbers in the midface might occur due to reduced proliferation,
95 increased cell death, or both. Cell proliferation remained unaffected (Extended Data Fig. 3),
96 however, we observed enhanced cell death in *Fgfr1*$^{cKO/cKO}$; *Fgfr2*$^{cKO/cKO}$; *ROSA26*$^{mT/mG}$ E10.5
97 mutants in the craniofacial mesenchyme, notably in the Lateral Nasal Process (LNP) relative to
98 the Medial Nasal Process (MNP; Fig. 1C, D). We next asked to what extent this observation could
99 explain the overall morphological defects. The BH3-only protein BIM plays a critical role in
100 initiating apoptotic pathway in multiple cell types by binding and repressing the function of several
101 pro-survival BCL-2 family members [12-14], and is involved in craniofacial development [15]. Consistent
102 with a role for cell survival in the etiology of craniofacial defects, we found that *Fgfr1*$^{cKO/cKO}$;

103 *Fgfr2*$^{cKO/+}$; *Bim*$^{+/-}$ E17.5 mutants exhibited a 55% reduction in midline separation along with a
104 partial rescue of medial skeletal structures, including the anterior nasal cartilage, palatine process,
105 premaxilla, primary and secondary palate, pterygoid process and basisphenoid bone, compared
106 to control embryos (Fig. 1E). The reduction in *Bim* levels significantly rescued defects particularly
107 at the level of the nasal mesenchyme and the midface (Fig. 1F and Supplementary Information
108 Fig. 1E). BIM is a known target of phosphorylation by several MAP kinases, particularly ERK1/2
109 which targets it for ubiquitination and proteasomal degradation [16]. JNK and PI3K/AKT activation
110 are also known to affect BIM levels [17]. Cell survival through BIM may therefore be regulated by
111 FGF since several of these signaling pathways are engaged by FGFR1 and FGFR2 [5]. Taken
112 together, these results underscore the importance of cell death in the conditional double null
113 mutant phenotype.
114

115 **Combined *Fgfr1/2* signaling mutations do not recapitulate the null phenotypes**

116 To interrogate signaling mechanisms *in vivo*, we generated an allelic series of knock-in
117 point mutations at the *Fgfr2* locus preventing binding of effectors to the receptor (Fig. 2A-B;
118 Extended Data Fig. 4), similar to previous *Fgfr1* mutations [7]. The *Fgfr2*^{F}, *Fgfr2*^{C}, and *Fgfr2*^{PG}
119 mutations were designed to disrupt binding of FRS2, CRK-L and PLCγ/GRB14, respectively. We
120 also generated compound *Fgfr2*^{CPG} and *Fgfr2*^{FCPG} signaling mutants by combining multiple
121 signaling mutations. Co-immunoprecipitation and western blot analysis showed that each
122 signaling mutation disrupted effector binding (Fig. 2B). *Fgfr2* signaling mutant alleles were
123 evaluated for their ability to partially or completely recapitulate the *Fgfr2*$^{-/-}$ E10.5 placenta and limb
124 phenotype [18-20]. Surprisingly, all signaling allele mutants were at least partially viable and fertile
125 as homozygotes (Supplementary Information Table S1 and Supplementary Information Fig. S2).
126 *Fgfr2*$^{F/F}$ and *Fgfr2*$^{FCPG/FCPG}$ homozygous mutants also exhibited defects in lacrimal gland
127 branching morphogenesis, a process regulated by FGF signaling [21,22] (Extended Data Fig. 5).
128 IRS2 has been found to bind FGFR2 [23], but no genetic interaction was observed between *Irs2*$^{-/-}$
129 and *Fgfr2*$^{FCPG/FCPG}$ mutants.

130 Because *Fgfr1* and *Fgfr2* are co-expressed in cNCCs, we reasoned that discrete functions
131 of signaling pathways downstream of one receptor could be masked by the presence of the other,
132 wild-type receptor. To test this hypothesis, we analyzed compound conditional hemizygous *Fgfr1*^{F},
133 *Fgfr1*^{FCPG} and *Fgfr2*^{F} mutations over the *Fgfr1*^{cKO} and *Fgfr2*^{cKO} conditional null alleles. *Fgfr1*$^{F/cKO}$;
134 *Fgfr2*$^{cKO/cKO}$ and *Fgfr1*$^{FCPG/cKO}$; *Fgfr2*$^{cKO/cKO}$ conditional mutants developed severe agenesis of
135 midface structures, nasal cartilage, and mandible but the phenotype was less severe than in
136 *Fgfr1*$^{cKO/cKO}$; *Fgfr2*$^{cKO/cKO}$ mutants. The nasal cartilage and mandible defects were further

137 exacerbated in *Fgfr1*$^{FCPG/cKO}$; *Fgfr2*$^{cKO/cKO}$ mutants (Fig. 2C, Extended Data Fig. 6A, red arrows,
138 and Supplementary Information Table S2). *Fgfr1*$^{cKO/cKO}$; *Fgfr2*$^{F/cKO}$ embryos developed more
139 severe midline fusion and mandible defects than *Fgfr1*$^{cKO/cKO}$; *Fgfr2*$^{cKO/+}$ controls. Similar to
140 *Fgfr1*$^{cKO/cKO}$; *Fgfr2*$^{cKO/cKO}$ mutants, morphological defects in *Fgfr1*$^{F/cKO}$; *Fgfr2*$^{cKO/cKO}$ and
141 *Fgfr1*$^{FCPG/cKO}$; *Fgfr2*$^{cKO/cKO}$ embryos arose as early as E10.5 and were accompanied by cell death
142 in the LNP (Extended Data Fig. 6B-E).

143 We next examined the importance of coordinate engagement of signaling pathways by
144 both receptors upon ligand activation. *Fgfr1*$^{C/C}$; *Fgfr2*$^{C/C}$ and *Fgfr1*$^{CPG/CPG}$; *Fgfr2*$^{CPG/CPG}$ double
145 mutants were recovered in normal numbers, fertile, and did not exhibit a craniofacial phenotype.
146 Compound *Fgfr1*$^{F/F}$; *Fgfr2*$^{+/F}$ mutants displayed hypoplastic nasal prominences and midline fusion
147 defects at E15.5 (Fig. 2D) with no defect in mandibular development (Extended Data Fig. 6F), but
148 *Fgfr1*$^{F/F}$; *Fgfr2*$^{F/F}$ mutant embryos were not recovered at E10.5. Similar hypoplastic nasal and
149 mandibular prominence defects were observed in *Fgfr1*$^{FCPG/FCPG}$; *Fgfr2*$^{+/FCPG}$ compound mutants
150 (Extended Data Fig. 6G). Interestingly, *Fgfr1*$^{FCPG/FCPG}$; *Fgfr2*$^{FCPG/FCPG}$ mutants survived to E7.5 and
151 still formed mesoderm, as evidenced by *Eomes* staining (Fig. 2E), in contrast to *Fgfr1*$^{-/-}$; *Fgfr2*$^{-/-}$
152 double mutants which fail at implantation on the same genetic background [24]. These results
153 indicate that signaling mutations in both *Fgfr1* and *Fgfr2* interact genetically during development,
154 but that the combination of the most severe signaling mutations fails to recapitulate the double
155 null mutant phenotype.
156

157 ### *Fgfr1/2* signaling mutations abrogate signal transduction cascades

158 FGFs activate numerous signaling pathways upon ligand stimulation [5]. To evaluate
159 intracellular pathway activation downstream of wild-type FGFR2, FGFR2^{F}, FGFR2^{CPG}, and
160 FGFR2^{FCPG}, we generated immortalized E10.5 frontonasal prominence cell lines (iFNPs) by
161 crossing to *Ink4a/Arf* mutants [25]. These cells express predominantly *Fgfr1* and to a lesser extent
162 *Fgfr2,* but no *Fgfr3* or *Fgfr4*. We then eliminated FGFR1 expression by CRISPR/Cas9
163 mutagenesis leaving FGFR2 as the sole receptor, and interrogated activation of six pivotal FGF-
164 engaged pathways [5] by FGF1, which gave more robust responses than FGF8b (Extended Data
165 Fig. 7) . For ERK1/2, but also for PI3K/AKT and PLCγ, robust activation seen in *wt*-iFNPs was
166 diminished in both *Fgfr2*$^{F/F}$ or *Fgfr2*$^{CPG/CPG}$-iFNPs, but only eliminated in *Fgfr2*$^{FCPG/FCPG}$ mutant cells
167 (Fig. 2F and Extended Data Fig. 8). Our data thus indicates that both FRS2 and CRKL/PLCγ
168 binding is necessary for activation of these pathways, as for *Fgfr1* [7]. P38, STAT3 and JNK
169 activation were also abrogated in *Fgfr2*$^{FCPG/FCPG}$-iFNPs, with variable effects in *Fgfr2*$^{F/F}$-iFNPs and
170 *Fgfr2*$^{CPG/CPG}$-iFNPs (Extended Data Fig. 8). Last, we revisited cell signaling pathways in

171 *Fgfr1*$^{FCPG/FCPG}$ mutants [7]. We used CRISPR/Cas9 to create *Fgfr1*$^{FCPG/FCPG}$; *Fgfr2*$^{CRISPR-KO}$-iFNP
172 cells, and found that both ERK1/2 and pAKT activation were eliminated in these cells (Extended
173 Data Fig. 8F-G). Together, these results indicate that the most severe signaling mutation
174 combinations in *Fgfr1* and *Fgfr2* effectively abrogate classic signal transduction pathways for each
175 receptor.
176
177 **_Fgfr2_ function requires its kinase activity**
178 The lack of more severe phenotypes in *Fgfr2* signaling mutants raised the possibility that
179 FGFR2 acts independent of kinase activity. To address this question, we generated a K517A
180 kinase dead (KD) mutation in the ATP binding site at the *Fgfr2* locus [26,27] (Fig. 2A and Extended
181 Data Fig. 4A, C). *Fgfr2*$^{KD/+}$ heterozygous embryos (27/60) showed no obvious defects at E10.5.
182 *Fgfr2*$^{KD/+}$ heterozygotes appeared normal during later developmental stages up to P0, but fewer
183 than expected (24/78) were recovered after weaning. They exhibited no limb or craniofacial
184 abnormalities, but significantly more severe semi-dominant defects in lacrimal gland development
185 than *Fgfr2*$^{F/F}$ and *Fgfr2*$^{FCPG/FCPG}$ mutants by P15 (Extended Data Fig. 5A-C).
186 No *Fgfr2*$^{KD/KD}$ homozygotes were recovered at birth (Supplementary Information Table S1).
187 Morphological examination of *Fgfr2*$^{KD/KD}$ embryos at E10.5 showed characteristic *Fgfr2*$^{-/-}$
188 phenotypes, with absence of limb buds, incomplete connection of the allantois to the ectoplacental
189 cone, and dilated pericardium (Fig. 3A), suggesting that FGFR2 broadly operates in a kinase-
190 dependent fashion. Moreover, since the *Fgfr2b* constitutive mutation leads to similar limb
191 phenotypes but no placental insufficiency [11], and phenotypes in both tissues are observed in
192 *Fgfr2*$^{-/-}$ or *Fgfr2*$^{KD/KD}$ mutants, FGFR2 activity must be kinase-dependent in both mesenchymal
193 and epithelial contexts. However, *Fgfr2*$^{KD/KD}$ embryos exhibited additional phenotypes including
194 severe posterior truncations and craniofacial defects (Fig. 3A). We tested for complementation
195 between *Fgfr2*^{KD} and *Fgfr2*$^{-}$ alleles to evaluate phenotypic differences. *Fgfr2*$^{KD/-}$ embryos showed
196 absence of limb buds and defects in the chorio-allantoic junction, along with dilated pericardium,
197 similar to *Fgfr2*$^{-/-}$ embryos, and posterior truncations defects similar to *Fgfr2*$^{KD/KD}$ embryos (Fig.
198 3A). In contrast, defects in the forebrain, medial and lateral nasal prominences, and maxillary and
199 mandibular prominences appeared less severe than in *Fgfr2*$^{KD/KD}$ mutants (Fig. 3B-D).
200 FGFRs can form heterodimers in culture [27,28], although these have never been
201 demonstrated *in vivo* in the absence of over-expression. The semi-dominant effects observed in
202 *Fgfr2*$^{KD/+}$ heterozygous mutants affecting postnatal lacrimal gland development, and the
203 craniofacial and mesoderm defects observed in *Fgfr2*$^{KD/KD}$ embryos suggest that the *Fgfr2*^{KD} allele
204 not only inactivates *Fgfr2* but also suppresses *Fgfr1* activity through FGFR2^{KD}:FGFR1

205 heterodimers, wherever they are co-expressed. This would explain why *Fgfr2*^{KD} mutants still
206 generally resemble *Fgfr2*$^{-/-}$ mutants which are lethal at a similar stage, rather than *Fgfr1*$^{-/-}$ mutants
207 [7,18,24]. While signaling might occur through heterodimers, this mechanism cannot fully account for
208 the discrepancy between FCPG and null phenotypes for either receptor, as *Fgfr1*$^{FCPG/FCPG}$;
209 *Fgfr2*$^{FCPG/FCPG}$ double mutants develop until E7.5 with a significant degree of mesoderm formation
210 (Fig. 2E) whereas *Fgfr1; Fgfr2* double null mutants have a more severe defect at implantation [18,24].
211 Alternatively, the FGFR2^{KD} receptor could act as a dominant negative by titrating/sequestering
212 ligand away from functional receptors, if it is distributed differently in the cell, but this is unlikely
213 as *Fgfr2*$^{FCPG/+}$ mutants do not show dominant negative effects and both knock-in alleles should
214 be expressed at similar levels.
215

216 **Cell matrix and cell adhesion properties are retained beyond canonical signaling**

217 Since signaling mutant cells showed near complete inactivation of classic RTK signaling
218 activities, but the corresponding mutant mice failed to recapitulate the null mutant phenotype, we
219 reasoned that some function engaged by FGF signaling must be retained in the most severe
220 *FCPG* mutants. Previous lines of evidence have implicated FGF signaling in the control of cell-
221 matrix [29] or cell-cell adhesion [24,30,31]. We examined *Fgfr1*; *Fgfr2* dependent cell
222 spreading/migration on extracellular matrix across a wound, using primary *Fgfr1*$^{cKO/+}$; *Fgfr2*$^{cKO/+}$,
223 *Fgfr1*$^{FCPG/+}$; *Fgfr2*$^{cKO/+}$, or *Fgfr1*$^{cKO/cKO}$; *Fgfr2*$^{cKO/cKO}$ FNP cells. Spreading of control cells over the
224 wound over twelve hours was comparable upon FGF, PDGF, and serum stimulated conditions.
225 Interestingly, *Fgfr1*$^{FCPG/cKO}$; *Fgfr2*$^{cKO/cKO}$ cells showed comparable spreading capacities in all three
226 stimulation conditions. However, *Fgfr1*$^{cKO/cKO}$; *Fgfr2*$^{cKO/cKO}$ double mutant cells failed to spread into
227 the wound area in response to FGF, while responses to PDGF and serum were normal (Fig. 4A).
228 We next investigated focal adhesion formation and found that GFP^{+} *Fgfr1*$^{cKO/+}$; *Fgfr2*$^{cKO/+}$;
229 *ROSA26*$^{mT/mG}$ control cells and *Fgfr1*$^{FCPG/cKO}$; *Fgfr2*$^{cKO/cKO}$; *ROSA26*$^{mT/mG}$ mutant cells formed
230 numerous Paxillin enriched focal adhesions in response to FGF, PDGF or serum. Double null
231 mutant cells however failed to form any Paxillin^{+} foci upon FGF treatment, but still responded
232 normally to PDGF and serum as expected (Fig. 4B and Extended Data Fig. 9A). Western blot
233 analysis showed reduced pFAK and total Paxillin levels in *Fgfr1*$^{cKO/cKO}$; *Fgfr2*$^{cKO/cKO}$ cells compared
234 to *Fgfr1*$^{cKO/+}$; *Fgfr2*$^{cKO/+}$ or *Fgfr1*$^{FCPG/cKO}$; *Fgfr2*$^{cKO/cKO}$ cells, and FAK phosphorylation depended on
235 FGF (Extended Data Fig. 9B-D). Likewise, we analyzed *Fgfr1*$^{CRISPR-KO}$; *Fgfr2*$^{+/+}$ and *Fgfr1*$^{CRISPR-KO}$;
236 *Fgfr2*$^{FCPG/FCPG}$ -iFNP cells and found that they spread and formed Paxillin^{+} focal adhesions in
237 response to serum, PDGF, or FGF, in contrast to *Fgfr1*$^{CRISPR-KO}$; *Fgfr2*$^{-/-}$ -iFNP cells (Fig. 4B and
238 Extended Data Fig. 9E). These observations indicate that although FGFR1^{FCPG} and FGFR2^{FCPG}

239 lose most FGF-dependent intracellular kinase signaling outputs, they still retain functions
240 pertaining to cell-matrix interactions and that cell spreading and stabilization of cell-matrix
241 interactions are actively governed by FGF signaling to its receptors.

242 We also explored if *Fgfr1*^{FCPG} cells established stable cell-cell contacts comparable to
243 control cells. We found extensive adherens junctions among *Fgfr1*$^{cKO/+}$; *Fgfr2*$^{cKO/+}$; *ROSA26*$^{mT/mG}$
244 control cells and *Fgfr1*$^{FCPG/cKO}$; *Fgfr2*$^{cKO/cKO}$; *ROSA26*$^{mT/mG}$ cells, marked by localized β-catenin
245 along cell boundaries (Fig. 5A-B and Extended Data Fig. 9F). In contrast, double null mutant cells
246 showed far fewer cell-cell contacts with no localized β-catenin accumulation, suggesting that
247 contacts are either unstable or do not mature (Fig. 5B). Last, we examined cell-cell contacts *in*
248 *vivo*, in the E11.5 LNP. GFP^{+} cNCCs in the mesenchyme exhibited extensive cell-cell contacts
249 within the LNP in both control and *Fgfr1*$^{FCPG/cKO}$; *Fgfr2*$^{cKO/cKO}$; *ROSA26*$^{mT/mG}$ embryos. Strikingly,
250 GFP^{+} cNCCs in the double null mutant LNP were mostly isolated and interspersed, whereas cell
251 contacts in the MNP remained unaffected (Fig. 5C). Taken together, these results indicate that
252 the most severe signaling mutations in *Fgfr1* and *Fgfr2* still retain cell-matrix and cell-cell
253 interactions otherwise lost in the nulls, while abrogating classic signal transduction pathways.
254

255 **Discussion**

256 FGFs are best known for activating signal transduction cascades, most prominently
257 ERK1/2 [5,6], Surprisingly, we find that mutations in *Fgfr1* and *Fgfr2* which broadly eliminate classic
258 RTK signaling outputs fail to recapitulate the *Fgfr1*$^{-/-}$ or *Fgfr2*$^{-/-}$ phenotypes. The near complete
259 abrogation of multiple signal transduction outputs in the most severe *Fgfr1* and *Fgfr2* signaling
260 alleles indicates that we have interrogated relevant cell signaling pathways and implies the
261 existence of non-canonical functions not impacted by our signaling mutations. Importantly, while
262 the *FCPG* mutations disrupt the ability of intracellular effectors to engage classical RTK activity,
263 they do not abrogate the receptor's kinase activity, suggesting that FGFR1^{FCPG} and FGFR2^{FCPG}
264 receptors may be able to phosphorylate other targets.

265 A wide body of literature has implicated FGFRs in cell adhesion through interactions of
266 the extracellular domain, which remains untouched in any of our signaling mutations, with cell
267 adhesion molecules. FGF ligand binding to FGFRs is known to involve a third party, heparan
268 sulfate proteoglycans (HSPGs)[32,33, 34], which in turn interact with integrins, regulating cell-matrix
269 adhesion [35-37]. Consistent with a critical role for FGFRs, we found that cell-matrix adhesion was
270 unperturbed in cells carrying the most severe signaling mutations, but lost in the absence of
271 FGFRs following FGF stimulation. Because FGF ligand still promotes cell-matrix adhesion in cells
272 derived from *Fgfr1/2*^{FCPG} mutants, the activity of cell adhesion receptors must be enhanced

273 independent of traditional signaling outputs, either directly through their interaction with FGFRs
274 or indirectly by an unknown molecule/kinase. Defects in FGF-dependent adhesion could also
275 result in the induction of anoikis [38], a process previously shown to be regulated by *Bim* [39],
276 potentially linking our observed adhesion defects and increase in cell death in the LNP. Last, focal
277 adhesion assembly and phosphorylation defects have also been observed in *Fgfr1*$^{-/-}$; *Fgfr2*$^{-/-}$
278 keratinocytes [29], suggesting that engagement of FGF signaling has a broad function in regulating
279 cell adhesion in both mesenchymal and epithelial contexts. Other receptor tyrosine kinases, like
280 PDGFRs, have been found to bind integrins [40] and PDGFR signaling mutations have also failed
281 to recapitulate null mutant phenotypes [41,42].

282 In addition, both FGFR1 and FGFR2 are known to interact through their extracellular
283 domain acid box with various cell adhesion molecules such as cadherins [43], critical players in
284 cNCC migration [44]. Consistent with a role for FGFRs in mediating cell-cell adhesion through
285 cadherins, we observed that cells derived from the most severe cell signaling mutants made
286 strong β-catenin cell contacts, in contrast to double null mutant cells. We also observed fewer
287 contacts *in vivo*, where double null mutant cells showed very limited interactions in the LNP.
288 FGFR1/2 association with cadherins may thus have a dual role, one in promoting cell motility
289 through FGF-induced ERK1/2 signaling [43], and an opposite one in cell adhesion, as ERK1/2
290 signaling is abrogated in *Fgfr1*^{FCPG} and *Fgfr2*^{FCPG} mutants. FGF signaling regulates E-cadherin
291 localization, and in the absence of *Fgfr1*, E-cadherin polarization is affected in mural
292 trophectoderm [24], *Drosophila* mesoderm [31], and zebrafish cardiomyocytes [30]. FGF signaling also
293 regulates cadherin switching during epithelial to mesenchymal transition, including neural crest
294 cell delamination [45-47]. Taken together, our results indicate that FGFRs regulate cell adhesion,
295 and possibly other processes, beyond their classic signaling cascades (Fig. 5D). Additional
296 genetic, biochemical and cell biological studies may identify further non-canonical roles for these
297 receptors beyond their traditional activities in signal transduction.

298 ***Acknowledgments.*** We thank Jia Li and Chantel Dixon for technical assistance; Kevin Kelley for
299 stable tissue culture facilities; Elaine Fuchs for helpful insights into cell adhesion mechanisms;
300 Jerry Chipuk for conversations about cell death; and our laboratory colleagues, Stu Aaronson,
301 Rob Krauss, and Sergei Sokol for critical comments on the manuscript. We thank the NYU School
302 of Dentistry Micro-CT Core and the Mt. Sinai Flow Cytometry and Microscopy facilities for
303 assistance and advice. C.J.D was supported by F32 DE026678 from NIH/NIDCR. This work was
304 supported in part by the Tisch Cancer Institute at Mount Sinai (P30 CA196521 Cancer Center
305 Support Grant, for access to Mt. Sinai cores) and by grant RO1 DE022778 from NIH/NIDCR to
306 P.S.

307

Figures, Extended Figures and Supplementary Information

Figure 1

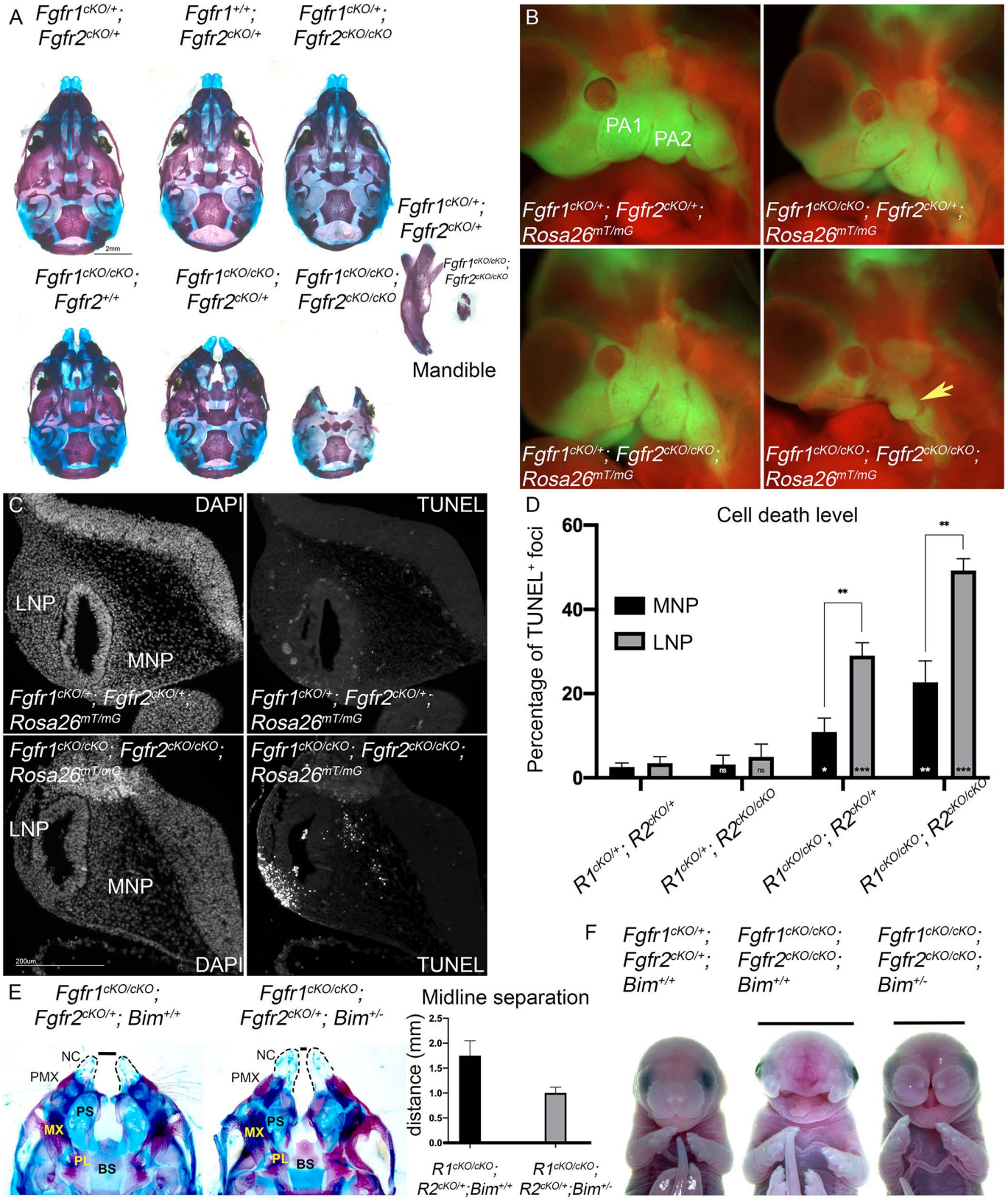
A
Fgfr1cKO/+; Fgfr2cKO/+
Fgfr1+/+; Fgfr2cKO/+
Fgfr1cKO/+; Fgfr2cKO/cKO
2mm
Fgfr1cKO/+; Fgfr2cKO/+
Fgfr1cKO/cKO; Fgfr2cKO/cKO
Fgfr1cKO/cKO; Fgfr2+/+
Fgfr1cKO/cKO; Fgfr2cKO/+
Fgfr1cKO/cKO; Fgfr2cKO/cKO
Mandible
B
PA1
PA2
Fgfr1cKO/+; Fgfr2cKO/+; Rosa26mT/mG
Fgfr1cKO/cKO; Fgfr2cKO/+; Rosa26mT/mG
Fgfr1cKO/+; Fgfr2cKO/cKO; Rosa26mT/mG
Fgfr1cKO/cKO; Fgfr2cKO/cKO; Rosa26mT/mG
C
DAPI
TUNEL
LNP
MNP
Fgfr1cKO/+; Fgfr2cKO/+; Rosa26mT/mG
Fgfr1cKO/cKO; Fgfr2cKO/cKO; Rosa26mT/mG
200um
D
Cell death level
Percentage of TUNEL+ foci
60
40
20
0
MNP
LNP
ns
*
**
***
R1cKO/+; R2cKO/+
R1cKO/+; R2cKO/cKO
R1cKO/cKO; R2cKO/+
R1cKO/cKO; R2cKO/cKO
E
Fgfr1cKO/cKO; Fgfr2cKO/+; Bim+/+
Fgfr1cKO/cKO; Fgfr2cKO/+; Bim+/-
NC
PMX
PS
MX
PL
BS
Midline separation
distance (mm)
2.5
2.0
1.5
1.0
0.5
0.0
R1cKO/cKO; R2cKO/+;Bim+/+
R1cKO/cKO; R2cKO/+;Bim+/-
F
Fgfr1cKO/+; Fgfr2cKO/+; Bim+/+
Fgfr1cKO/cKO; Fgfr2cKO/cKO; Bim+/+
Fgfr1cKO/cKO; Fgfr2cKO/cKO; Bim+/-

310 **Figure 1: Defects in craniofacial morphogenesis in *Fgfr1/2* double mutants.**

311 (A) Alcian blue/ alizarin red staining of mouse skulls at E18.5 showed a facial cleft in
312 *Fgfr1*$^{cKO/cKO}$ embryos, which was exacerbated in *Fgfr1*$^{cKO/cKO}$*; Fgfr2*$^{cKO/+}$ mutants. *Fgfr1*$^{cKO/cKO}$*;*
313 *Fgfr2*$^{cKO/cKO}$ mutants exhibited the most severe defect, with agenesis of proximal structures, as
314 well as severe reduction of the mandible.

315 (B) *Fgfr1*$^{cKO/cKO}$*; Fgfr2*$^{cKO/cKO}$; *ROSA26*$^{mT/mG}$ mutants showed fewer GFP^{+} cNCCs in the PA1
316 (yellow arrow), PA2 and migratory stream relative to control embryos at E10.5.

317 (C) Apoptosis was examined at E10.5 by TUNEL. Increased TUNEL positive cells were
318 observed *Fgfr1*$^{cKO/cKO}$*; Fgfr2*$^{cKO/cKO}$ mutants in the lateral nasal process (LNP) compared to
319 controls. Fewer TUNEL positive cells were observed in the medial nasal process (MNP).

320 (D) Quantitation of TUNEL positive foci across different mutant genotypes show a 40-fold
321 increase in cell death in *Fgfr1/2* double mutants in the LNP ("*" inside the bar graph represents
322 significance level compared to control) at E10.5.

323 (E) Inferior view (mandibles removed) of alcian blue/ alizarin red stained mouse skulls in
324 *Fgfr1*$^{cKO/cKO}$*; Fgfr2*$^{cKO/+}$*; Bim*$^{+/+}$ and *Fgfr1*$^{cKO/cKO}$*; Fgfr2*$^{cKO/+}$; *Bim*$^{+/-}$ embryos showed partial rescue
325 of medial structures, the nasal cartilage (NC) and palatine (PL) process, premaxilla (PMX), maxilla
326 (MX), basisphenoid (BS) and palatal shelves (PS) in *Bim*$^{-/+}$ mutants. Black bar (**-**) measures
327 midline separation. Average midline separation (mm) is reduced by 2-fold (N=4, P>0.0109) in
328 *Fgfr1*$^{cKO/cKO}$*; Fgfr2*$^{cKO/+}$; *Bim*$^{+/-}$ as represented in the graph.

329 (F) Frontal views of control *Fgfr1*$^{cKO/+}$*; Fgfr2*$^{cKO/+}$*; Bim*$^{+/+}$, *Fgfr1*$^{cKO/cKO}$*; Fgfr2*$^{cKO/cKO}$*; Bim*$^{+/+}$, and
330 *Fgfr1*$^{cKO/cKO}$*; Fgfr2*$^{cKO/cKO}$*; Bim*$^{+/-}$ embryos at E17.5 showing partial phenotypic rescue. Black bar (**-**)
331 indicates intercanthal distance.

332

333

Figure 2

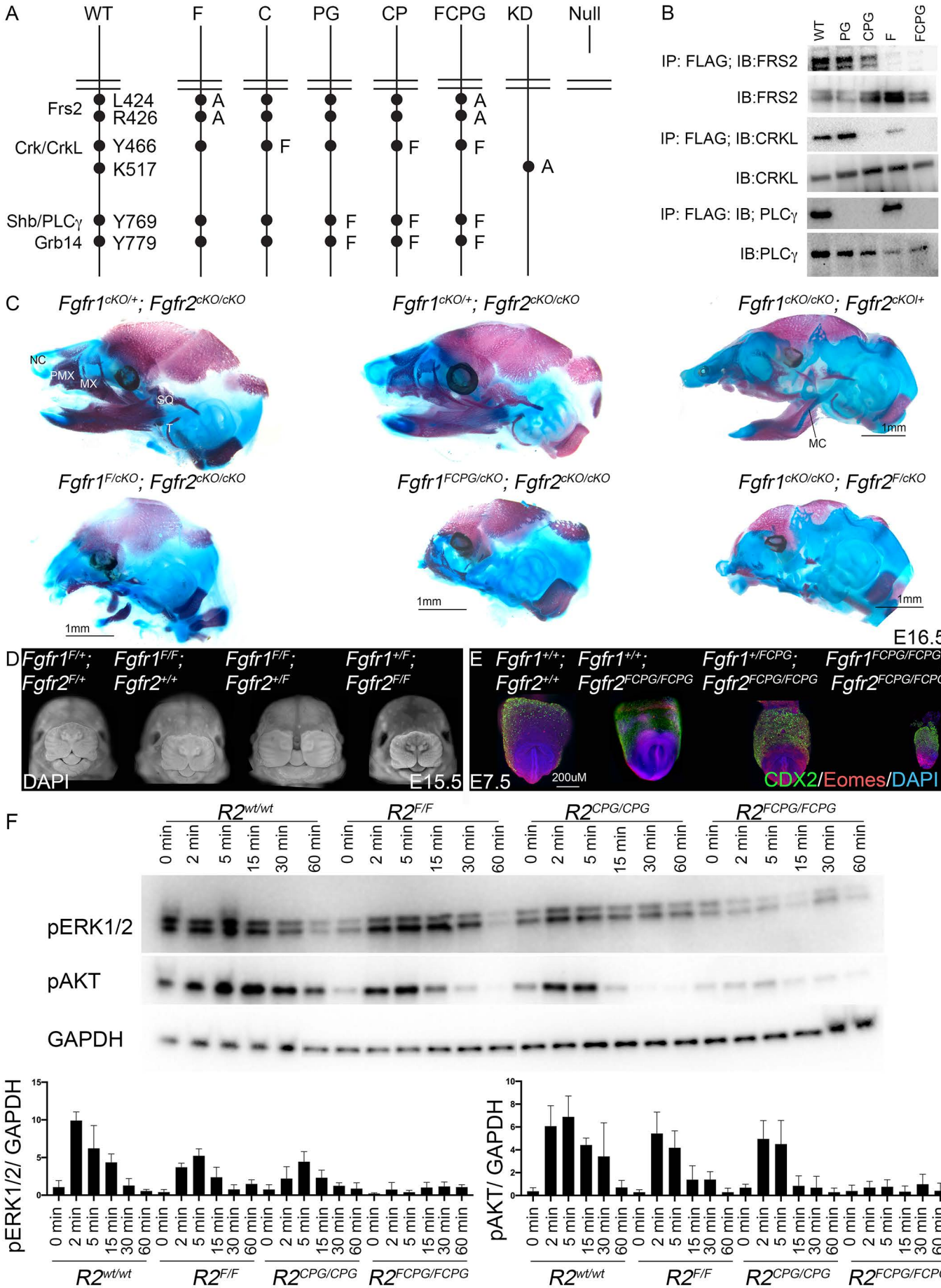
A
WT
F
C
PG
CP
FCPG
KD
Null
Frs2
L424
R426
Crk/CrkL
Y466
K517
Shb/PLCγ
Y769
Grb14
Y779
B
WT
PG
CPG
F
FCPG
IP: FLAG; IB:FRS2
IB:FRS2
IP: FLAG; IB:CRKL
IB:CRKL
IP: FLAG: IB; PLCγ
IB:PLCγ
C
Fgfr1cKO/+; Fgfr2cKO/cKO
Fgfr1cKO/+; Fgfr2cKO/cKO
Fgfr1cKO/cKO; Fgfr2cKOl+
NC
PMX
MX
SQ
T
MC
1mm
Fgfr1F/cKO; Fgfr2cKO/cKO
Fgfr1FCPG/cKO; Fgfr2cKO/cKO
Fgfr1cKO/cKO; Fgfr2F/cKO
E16.5
D
Fgfr1F/+; Fgfr2F/+
Fgfr1F/F; Fgfr2+/+
Fgfr1F/F; Fgfr2+/F
Fgfr1+/F; Fgfr2F/F
DAPI
E15.5
E
Fgfr1+/+; Fgfr2+/+
Fgfr1+/+; Fgfr2FCPG/FCPG
Fgfr1+/FCPG; Fgfr2FCPG/FCPG
Fgfr1FCPG/FCPG; Fgfr2FCPG/FCPG
E7.5
200uM
CDX2/Eomes/DAPI
F
R2wt/wt
R2F/F
R2CPG/CPG
R2FCPG/FCPG
0 min
2 min
5 min
15 min
30 min
60 min
pERK1/2
pAKT
GAPDH
pERK1/2/ GAPDH
pAKT/ GAPDH

334 **Figure 2: Coordinate roles *Fgfr1* and *Fgfr2* signaling mutation in development.**

335 (A) Schematic representation of the *Fgfr2* allelic series. Critical effectors that bind to FGFR2
336 are listed on the left of the $Fgfr2^{WT}$ allele (WT). Critical residues for this binding are annotated on
337 the right. Amino acid substitutions for each allele are provided to the right of all mutant alleles
338 generated.

339 (B) Co-immunoprecipitation experiments confirmed the ability of F, C and PG mutations to
340 disrupt FRS2, CRKL and PLCγ binding to FGFR2, respectively. Constructs expressing $Fgfr2^{WT}$,
341 $Fgfr2^{PG}$, $Fgfr2^{CPG}$, $Fgfr2^{F}$ and $Fgfr2^{FCPG}$-triple Flag-tag cDNA were overexpressed in 3T3 cells.
342 FLAG pull-downs were then immunoblotted to show interactions of FRS2, CRKL and PLCγ to
343 $FGFR2^{WT}$ and mutant receptors.

344 (C) Sagittal view of E16.5 alcian blue/ alizarin red stained skulls from control littermate (top)
345 and *Fgfr1* or *Fgfr2* signaling (bottom) mutants. In $Fgfr1^{F/cKO}$; $Fgfr2^{cKO/cKO}$ mutants, the frontal bone,
346 nasal cartilage (NC), squamosal bone (SQ), tympanic bulla (T), maxilla (MX) and mandible (MD)
347 were affected. $Fgfr1^{FCPG/cKO}$; $Fgfr2^{cKO/cKO}$ mutants showed a more severe defect. $Fgfr2^{F}$ signaling
348 mutants ($Fgfr1^{cKO/cKO}$; $Fgfr2^{F/cKO}$) showed defects in mandible along with reduced ossification of
349 the premaxilla (PMX) and maxilla and loss of the squamosal bone and tympanic bulla.

350 (D) DAPI stained frontal facial view for $Fgfr1^{F}$ and $Fgfr2^{F}$ mutant embryos at E15.5. $Fgfr1^{F/F}$;
351 $Fgfr2^{+/F}$ embryos showed a severe facial cleft compared to other genotypes.

352 (E) CDX2 and EOMES expression in $Fgfr1^{FCPG}$ and $Fgfr2^{FCPG}$ compound signaling mutants at
353 E7.5. In contrast to $Fgfr1^{-/-}$; $Fgfr2^{-/-}$ which fail to implant on the 129S4 co-isogenic background, we
354 could recover $Fgfr1^{FCPG/FCPG}$; $Fgfr2^{FCPG/FCPG}$ compound mutants at E7.5 but not at E10.5.
355 $Fgfr1^{FCPG/FCPG}$; $Fgfr2^{FCPG/FCPG}$ mutants were growth-retarded but expressed mesodermal EOMES
356 and the trophectoderm marker CDX2.

357 (F) iFNP cells ($Fgfr1^{CRISPR-KO}$) derived from the indicated genotypes, $Fgfr2^{wt/wt}$ ($R2^{wt/w}$), $Fgfr2^{F/F}$
358 ($R2^{F/F}$), $Fgfr2^{CPG/CPG}$ ($R2^{CPG/CPG}$) and $Fgfr2^{FCPG/FCPG}$ ($R2^{FCPG/FCPG}$), were stimulated with FGF1 for
359 the indicated times (0-60 mins) to analyze pERK1/2 and pAKT activation. Quantification of
360 pathway activation for pERK1/2 and pAKT, normalized to GAPDH, is reported as mean ± standard
361 deviation with a minimum of three independent biological replicates.

362

363

Figure 3

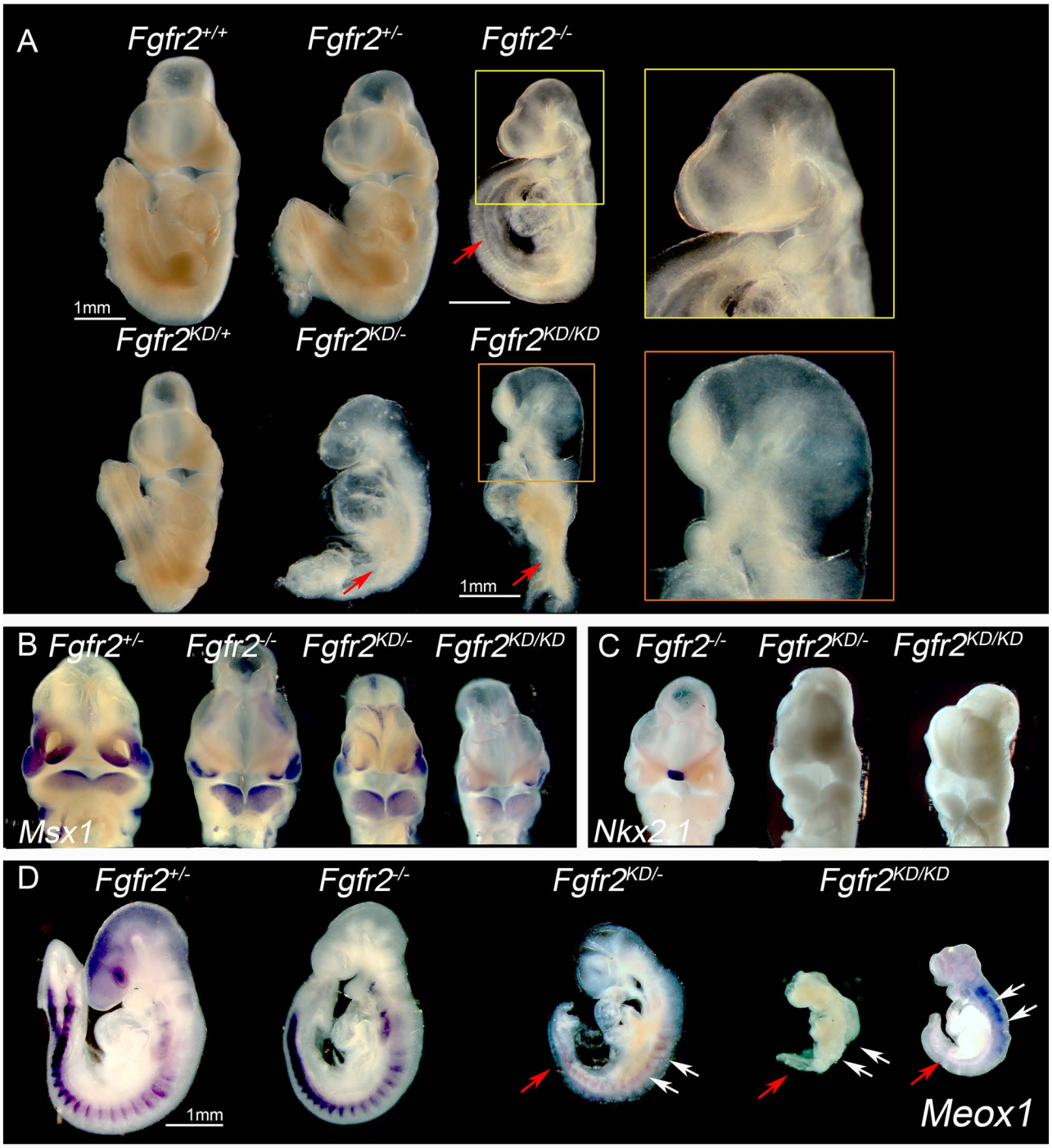
A
Fgfr2+/+
Fgfr2+/-
Fgfr2-/-
1mm
Fgfr2KD/+
Fgfr2KD/-
Fgfr2KD/KD
1mm
B Fgfr2+/-
Fgfr2-/-
Fgfr2KD/-
Fgfr2KD/KD
Msx1
C Fgfr2-/-
Fgfr2KD/-
Fgfr2KD/KD
Nkx2.1
D Fgfr2+/-
Fgfr2-/-
Fgfr2KD/-
Fgfr2KD/KD
1mm
Meox1

364 **Figure 3: A kinase dead mutation in *Fgfr2* recapitulates multiple aspects of the *Fgfr2*$^{-/-}$**
365 **phenotype.**
366 (A) Morphological examination of *Fgfr2* kinase dead phenotype at E10.5. *Fgfr2*$^{KD/-}$ and
367 *Fgfr2*$^{KD/KD}$ mutants had no limb buds (red arrows), and had defects in the allantois which was
368 loosely or incompletely held by the chorion to the ectoplacental cone, along with a dilated
369 pericardium similar to *Fgfr2*$^{-/-}$ mutants. Both *Fgfr2*$^{KD/-}$ and *Fgfr2*$^{KD/KD}$ mutants displayed severe
370 posterior truncations and *Fgfr2*$^{KD/KD}$ mutants showed a more severe phenotype. *Fgfr2*$^{KD/KD}$
371 mutants also displayed craniofacial defects with poorly developed facial prominences compared
372 to *Fgfr2*$^{KD/-}$ mutants.
373 (B) Wholemount mRNA *in situ* hybridization for cNCC mesenchyme marker *Msx1* at E10.5.
374 *Msx1* was expressed in the facial prominences (LNP, MNP and mandibular prominences) in *Fgfr2*$^{-}$
375 $^{/-}$ embryos at similar levels compared to control *Fgfr2*$^{+/-}$ embryo. *Msx1* expression was also
376 observed in *Fgfr2*$^{KD/-}$ mutants but was reduced in *Fgfr2*$^{KD/KD}$ mutants.
377 (C) Wholemount mRNA in situ hybridization for midline marker *Nkx2.1*. *Nkx2.1* was expressed
378 in the midline floor plate of *Fgfr2*$^{-/-}$ mutants, but not detected in *Fgfr2*$^{KD/-}$ and *Fgfr2*$^{KD/KD}$ mutants.
379 (D) *Meox1* mRNA expression in somites of E10.5 *Fgfr2*$^{+/-}$ embryos was comparable to *Fgfr2*$^{-/-}$
380 mutants, but severely reduced in both *Fgfr2*$^{KD/-}$ and *Fgfr2*$^{KD/KD}$ mutants (white arrows) along with
381 defects in axis elongation and posterior somite formation (red arrow).
382
383

Figure 4

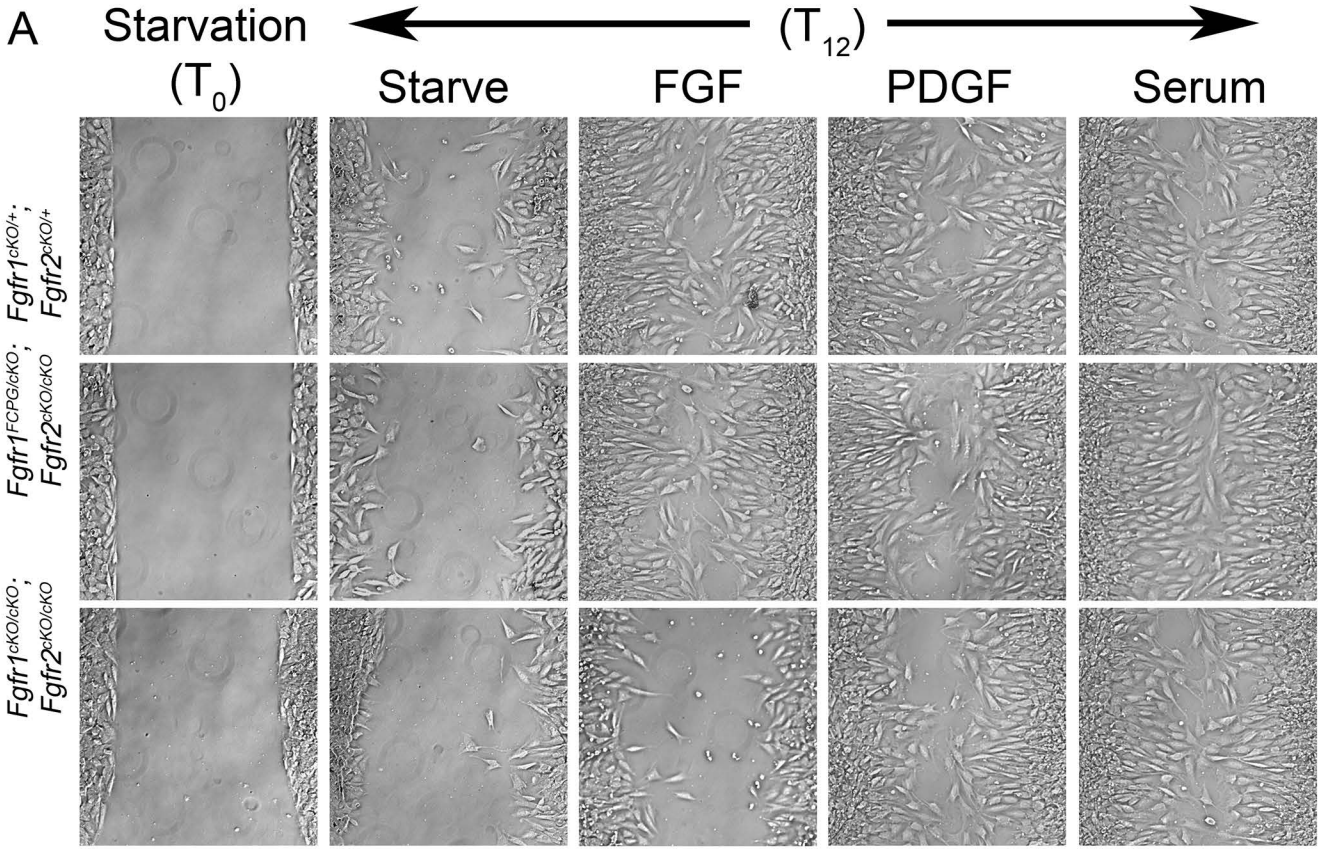
A
Starvation
(T_0)
(T_{12})
Starve
FGF
PDGF
Serum
Fgfr1cKO/+; Fgfr2cKO/+
Fgfr1FCPG/cKO; Fgfr2cKO/cKO
Fgfr1cKO/cKO; Fgfr2cKO/cKO

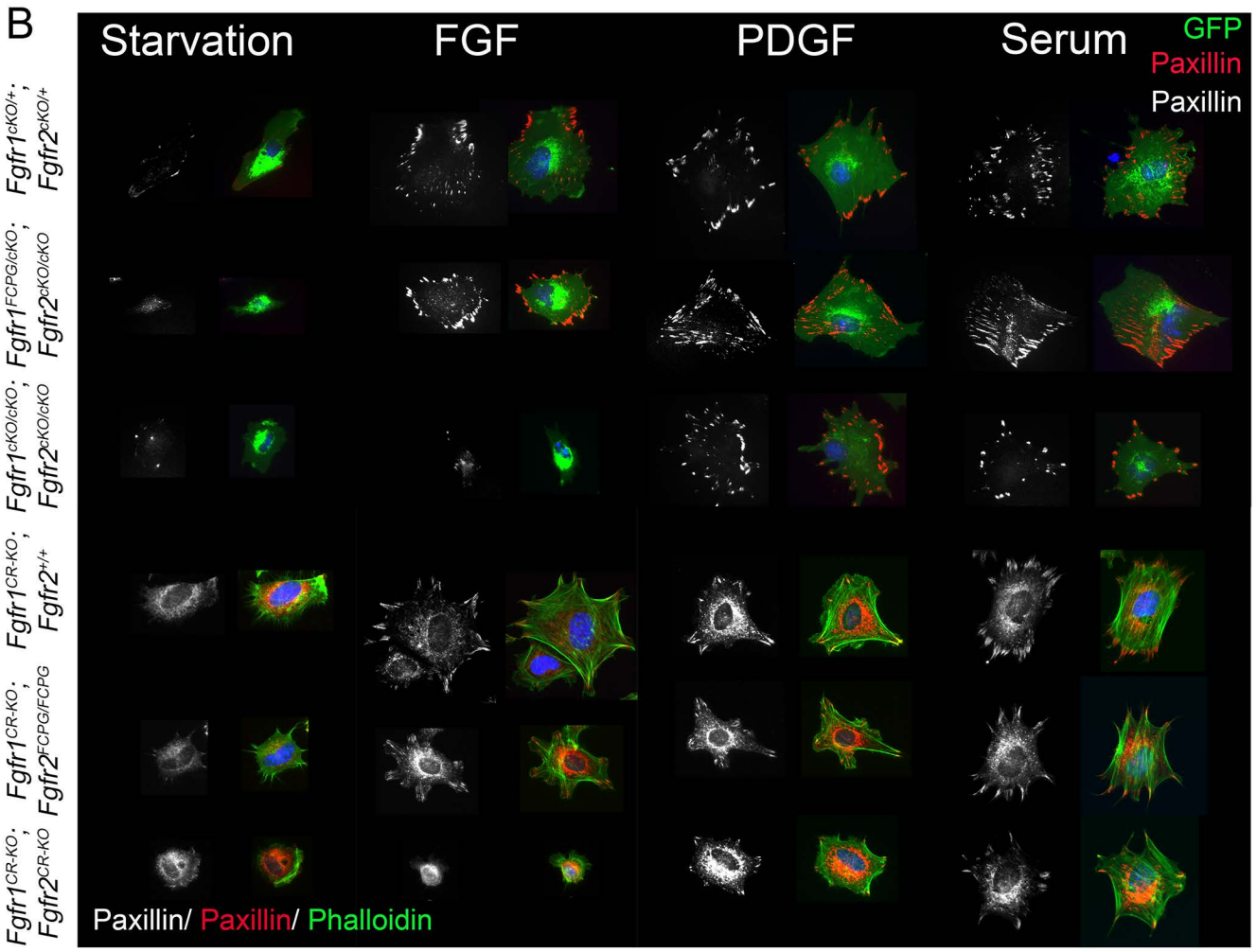
B
Starvation
FGF
PDGF
Serum
GFP
Paxillin
Paxillin
Fgfr1cKO/+; Fgfr2cKO/+
Fgfr1FCPG/cKO; Fgfr2cKO/cKO
Fgfr1cKO/cKO; Fgfr2cKO/cKO
Fgfr1CR-KO; Fgfr2+/+
Fgfr1CR-KO; Fgfr2FCPG/FCPG
Fgfr1CR-KO; Fgfr2CR-KO
Paxillin/ Paxillin/ Phalloidin

384 **Figure 4: Cell matrix adhesion properties are retained in FCPG mutants.**

385 (A) Scratch/wound healing assay was used to study cell spreading. Control (*Fgfr1*$^{cKO/+}$;
386 *Fgfr2*$^{cKO/+}$) and *Fgfr1*$^{FCPG/cKO}$; *Fgfr2*$^{cKO/cKO}$ primary FNP cells showed active spreading over 12
387 hours (T_{12}) in response to FGF1, PDGF-A, or serum. *Fgfr1*$^{cKO/cKO}$; *Fgfr2*$^{cKO/cKO}$ mutant cells showed
388 limited spreading upon FGF stimulation but normal spreading in response to PDGF or serum.

389 (B) Focal-adhesion formation was assayed by Paxillin immunostaining in *Fgfr1* and *Fgfr2*
390 signaling mutant primary FNP cells. GFP^{+} *Fgfr1*$^{cKO/+}$; *Fgfr2*$^{cKO/+}$; *ROSA26*$^{mT/mG}$ control,
391 *Fgfr1*$^{FCPG/cKO}$; *Fgfr2*$^{cKO/+}$; *ROSA26*$^{mT/mG}$, and *Fgfr1*$^{cKO/cKO}$; *Fgfr2*$^{cKO/cKO}$; *ROSA26*$^{mT/mG}$ mutant cells
392 were treated with FGF1, PDGFA or serum for 3 hours before analyzing Paxillin localization to
393 focal adhesions. In control cells and *Fgfr1*$^{FCPG/cKO}$; *Fgfr2*$^{cKO/+}$, we detected multiple Paxillin^{+} foci
394 upon FGF1, PDGFA, or serum stimulation. *Fgfr1*$^{cKO/cKO}$; *Fgfr2*$^{cKO/cKO}$; *ROSA26*$^{mT/mG}$ mutant FNP
395 cells failed to form focal adhesions in response to FGF, in contrast to PDGF or serum (quantified
396 in Extended Data Fig. 9A). Cell spreading properties were also analyzed for *Fgfr2*$^{WT/WT}$
397 (*Fgfr1*$^{CRISPR-KO}$; *Fgfr2*$^{WT/WT}$), *Fgfr2*$^{FCPG/FCPG}$ (*Fgfr1*$^{CRISPR-KO}$; *Fgfr2*$^{FCPG/FCPG}$), and *Fgfr2*$^{-/-}$ (*Fgfr1*$^{CRISPR-}$
398 ^{KO}; *Fgfr2* $^{CRISPR-KO}$) -iFNP cells in which *Fgfr1* was disrupted. Addition of FGF1, PDGFA or serum
399 resulted in robust cell spreading and formation of Paxillin^{+} focal adhesion in *Fgfr1*$^{CRISPR-KO}$;
400 *Fgfr2*$^{FCPG/FCPG}$ and *Fgfr1*$^{CRISPR-KO}$; *Fgfr2*$^{+/+}$ -iFNP cells. *Fgfr2*$^{-/-}$ (*Fgfr1*$^{CRISPR-KO}$; *Fgfr2* $^{CRISPR-KO}$) -iFNP
401 cells showed severe defects in focal adhesion formation upon FGF1 treatment, but was
402 unaffected in response to PDGFA or serum (quantified in Extended Data Fig. 9E).

403

Figure 5

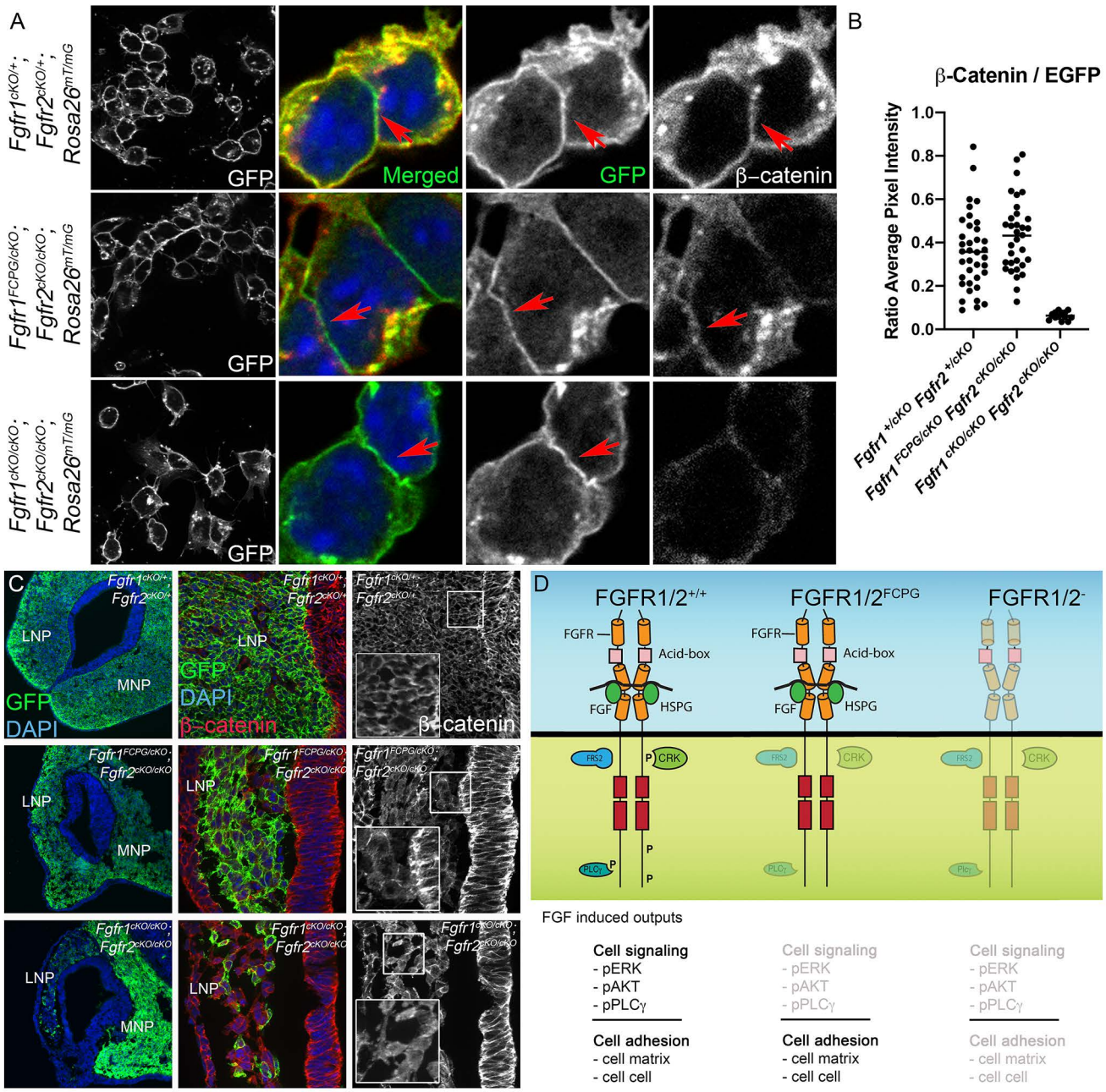
A
Fgfr1cKO/+; Fgfr2cKO/+; Rosa26mT/mG
Fgfr1FCPG/cKO; Fgfr2cKO/cKO; Rosa26mT/mG
Fgfr1cKO/cKO; Fgfr2cKO/cKO; Rosa26mT/mG
GFP
Merged
β–catenin
B
β-Catenin / EGFP
Ratio Average Pixel Intensity
1.0
0.8
0.6
0.4
0.2
0.0
Fgfr1+/cKO Fgfr2+/cKO
Fgfr1FCPG/cKO Fgfr2cKO/cKO
Fgfr1cKO/cKO Fgfr2cKO/cKO
C
LNP
MNP
GFP
DAPI
β–catenin
D
FGFR1/2+/+
FGFR1/2FCPG
FGFR1/2-
FGFR
Acid-box
FGF
HSPG
FRS2
CRK
P
PLCγ
FGF induced outputs
Cell signaling
- pERK
- pAKT
- pPLCγ
Cell adhesion
- cell matrix
- cell cell

404 **Figure 5: Cell-cell adhesion is retained in *Fgfr* signaling mutants.**

405 (A) GFP$^+$ primary FNP cells from control *Fgfr1*$^{cKO/+}$; *Fgfr2*$^{cKO/+}$; *ROSA26*$^{mT/mG}$ and *Fgfr1*$^{FCPG/cKO}$;
406 *Fgfr2*$^{cKO/cKO}$; *ROSA26*$^{mT/mG}$ embryos formed extensive cell-cell contacts, in contrast to *Fgfr1*$^{cKO/cKO}$;
407 *Fgfr2*$^{cKO/cKO}$; *ROSA26*$^{mT/mG}$ mutants. Quantification is provided in Extended Data Fig. 9F. β-
408 catenin was localized along the cell contact boundaries in GFP$^+$ FNP cells from control and
409 *Fgfr1*$^{FCPG/cKO}$; *Fgfr2*$^{cKO/cKO}$; *ROSA26*$^{mT/mG}$ embryos in contrast to *Fgfr1*$^{cKO/cKO}$; *Fgfr2*$^{cKO/cKO}$;
410 *ROSA26*$^{mT/mG}$ mutants.

411 (B) β-catenin immunofluorescence was quantified and represented as mean for each
412 genotype.

413 (C) Extensive cell-cell contacts with β-catenin localization (insets) were observed *in vivo* in
414 control *Fgfr1*$^{cKO/+}$; *Fgfr2*$^{cKO/+}$; *ROSA26*$^{mT/mG}$ and *Fgfr1*$^{FCPG/cKO}$; *Fgfr2*$^{cKO/cKO}$; *ROSA26*$^{mT/mG}$ cells in
415 both developing LNP and MNP at E11.5. In contrast, *Fgfr1*$^{cKO/cKO}$; *Fgfr2*$^{cKO/cKO}$; *ROSA26*$^{mT/mG}$
416 double null mutants GFP$^+$ cells remained sparse in the LNP and showed no localized β-catenin.

417 (D) Model of FGF-mediated cell signaling pathways. In wild-type (WT) cells, activation by
418 FGFs engages a canonical RTK signal transduction pathway, leading for the activation of ERK1/2,
419 PI3K/AKT, PLCγ, and additional pathways. In addition, FGFs activate non-canonically both cell-
420 matrix as well as cell-cell adhesion, in a kinase-dependent manner, possibly facilitated through
421 interactions of the FGF receptors through their extracellular domain with cell adhesion receptors.
422 *Fgfr1*^{FCPG} or *Fgfr2*^{FCPG} mutant cells fail to activate a classical RTK signal transduction pathway
423 (light grey) but can still promote cell adhesion (black), as their kinase activity has not been
424 disrupted. In null mutant cells, neither FGF-induced cell signaling nor cell adhesion are observed
425 (light grey), since the receptors are not expressed.

Extended Data Figure 1

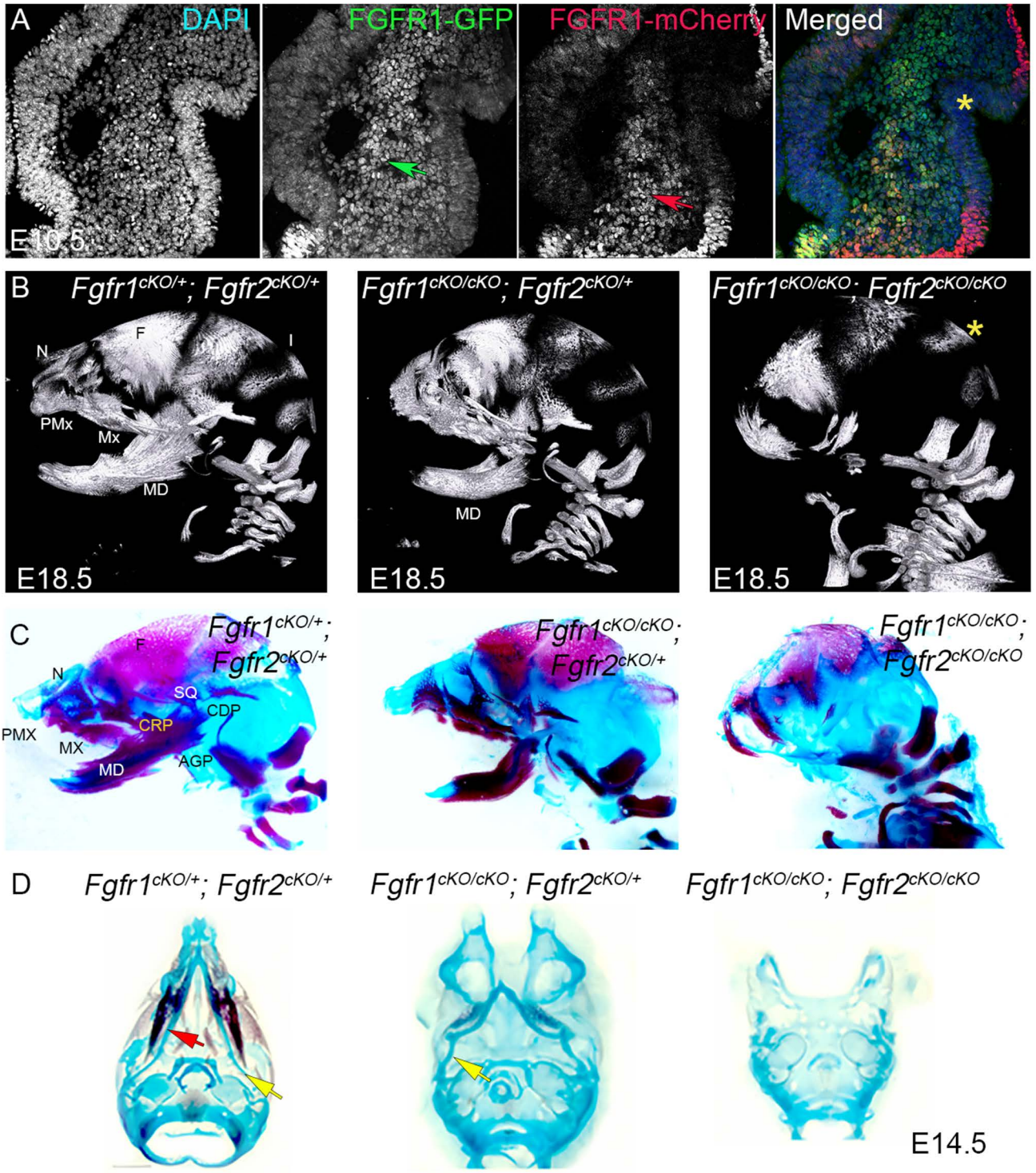

426 **Extended Data Fig. 1: Defects in craniofacial morphogenesis in *Fgfr1*$^{cKO/cKO}$; *Fgfr2*$^{cKO/cKO}$**
427 **double mutants.**
428 (A) Spatial domain of FGFR1 and FGFR2 expression in facial prominences at E10.5. GFP
429 and mCherry immunohistochemistry were used to detect expression from *Fgfr1-GFP* and *Fgfr2-*
430 *mCherry* reporter alleles. GFP expression was primarily restricted to the mesenchyme (green
431 arrow). Although mCherry expression was restricted to the epithelium, many cells in the
432 mesenchyme also express mCherry (red arrow). mCherry expression is downregulated in the
433 epithelium lining the nasal pit (yellow asterisk). FGFR1 and FGFR2 co-expression in the
434 craniofacial skeleton is also observed E17.5 (Supplementary Information Fig. S1a).
435 (B) Micro-CT analysis of ossified structures in the head at E18.5. An overall reduction or
436 complete loss of ossification of cNCC-derived facial bones in *Fgfr1/2* conditional double mutant
437 is seen compared to the control. Frontal (F) and nasal bones (N), pre-maxilla (PMX) and maxilla
438 (MX) were severely affected. Mesoderm derived bones including parietal and interparietal (I)
439 bones remained unaffected (yellow asterisk). *Fgfr1*$^{cKO/cKO}$; *Fgfr2*$^{cKO/+}$ mutants showed an overall
440 reduction in the size of the mandible (MD), with the proximal structures most severely affected. A
441 more detailed morphometry analysis regarding changes in skull length, intercanthal distance,
442 length of frontal bone and length of nasal cartilage at E18.5 for different genotypes is provided in
443 Supplementary Information Fig S1B.
444 (C) Sagittal view of alcian blue/ alizarin red stained mouse skull at E16.5 for different
445 genotypes. Frontal (F) and nasal (N) bone, mandible (MD), premaxilla (PMX), maxilla (MX) and
446 the squamous (SQ) bone was severely affected in *Fgfr1*$^{cKO/cKO}$; *Fgfr2*$^{cKO/cKO}$ conditional double
447 mutants. In *Fgfr1*$^{cKO/cKO}$; *Fgfr2*$^{cKO/+}$ mutants also showed partial mandibular defect where proximal
448 condylar (CDP), coronoid (CRP) and angular process (AGP) of the mandible was affected.
449 (D) Alcian blue/ alizarin red staining of mouse skulls at E14.5. Alizarin red staining mark
450 ossified region in mandible and maxilla in control (*Fgfr1*$^{cKO/+}$; *Fgfr2*$^{cKO/+}$) skull. Yellow arrowhead
451 marks the Meckel's cartilage. In *Fgfr1*$^{cKO/cKO}$; *Fgfr2*$^{cKO/+}$ mutants, we observed reduced ossification
452 (red arrow) in the mandible with a significantly smaller Meckel's cartilage (yellow arrow). Meckel's
453 cartilage was lost in *Fgfr1/2* conditional double mutant with no observable ossification.
454
455

Extended Data Figure 2

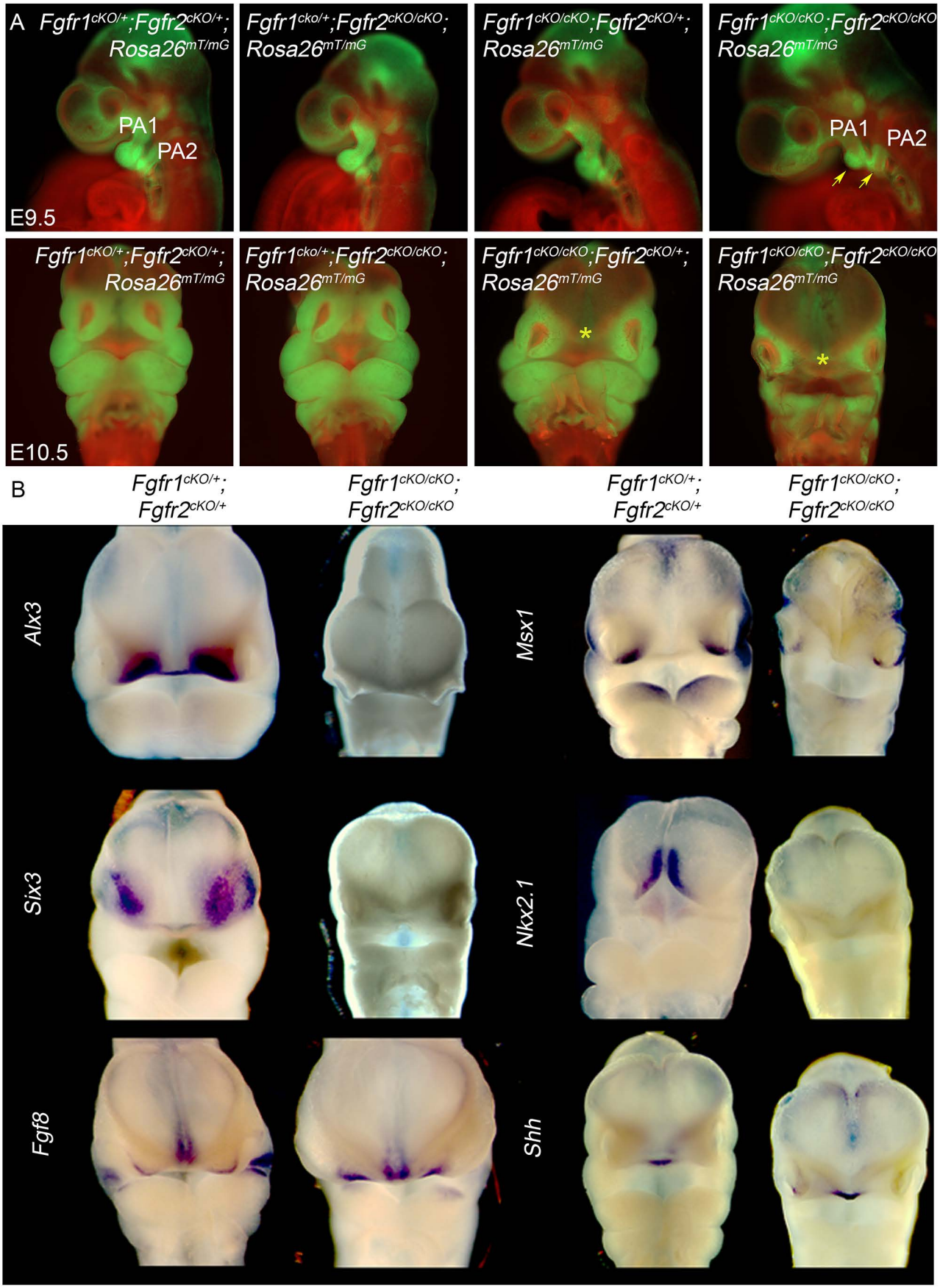

456 **Extended Data Fig. 2: Molecular changes and defects in craniofacial ossification in**
457 ***Fgfr1$^{cKO/cKO}$; Fgfr2$^{cKO/cKO}$* double mutants.**
458 (A) Conditional *Fgfr1-Fgfr2* null mutant embryos carrying the *ROSA26$^{mT/mG}$* reporter analyzed
459 in whole mount. cNCCs in the head express GFP (green). At E9.5 (top panel), *Fgfr1/2* conditional
460 double mutants (*Fgfr1$^{cKO/cKO}$; Fgfr2$^{cKO/cKO}$*; *ROSA26$^{mT/mG}$*) had hypoplastic pharyngeal arches PA1
461 and PA2 (yellow arrows), shown by reduced GFP fluorescence compared to *Fgfr1-Fgfr2*
462 conditional heterozygotes. *Fgfr1$^{cKO/+}$; Fgfr2$^{cKO/cKO}$* and *Fgfr1$^{cKO/cKO}$; Fgfr2$^{cKO/+}$* mutants appeared
463 normal at this stage. Frontal view at E10.5 (lower panels). A wide midline separation was
464 observed in both *Fgfr1/2* conditional double (*Fgfr1$^{cKO/cKO}$; Fgfr2$^{cKO/cKO}$*; *ROSA26$^{mT/mG}$*) and
465 *Fgfr1$^{cKO/cKO}$; Fgfr2$^{cKO/+}$*; *ROSA26$^{mT/mG}$* mutants (yellow asterisk) compared to controls and
466 *Fgfr1$^{cKO/+}$; Fgfr2$^{cKO/cKO}$*; *ROSA26$^{mT/mG}$* mutants.
467 (B) Whole mount mRNA *in situ* hybridization was used to compare the expression of *Alx3,*
468 *Msx1, Six3, Nkx2.1, Fgf8* and *Shh* at E10.5 in the facial primordia for *Fgfr1$^{cKO/+}$; Fgfr2$^{cKO/+}$* control
469 and *Fgfr1$^{cKO/cKO}$; Fgfr2$^{cKO/cKO}$* mutants. *Msx1* expression was reduced, and *Alx3*, *Six3* and *Nkx2.1*
470 expression were lost in *Fgfr1/2* conditional double mutants. The expression of *Fgf8* and *Shh*
471 remained unaffected in the *Fgfr1$^{cKO/cKO}$; Fgfr2$^{cKO/cKO}$* mutants.
472
473

Extended Data Figure 3

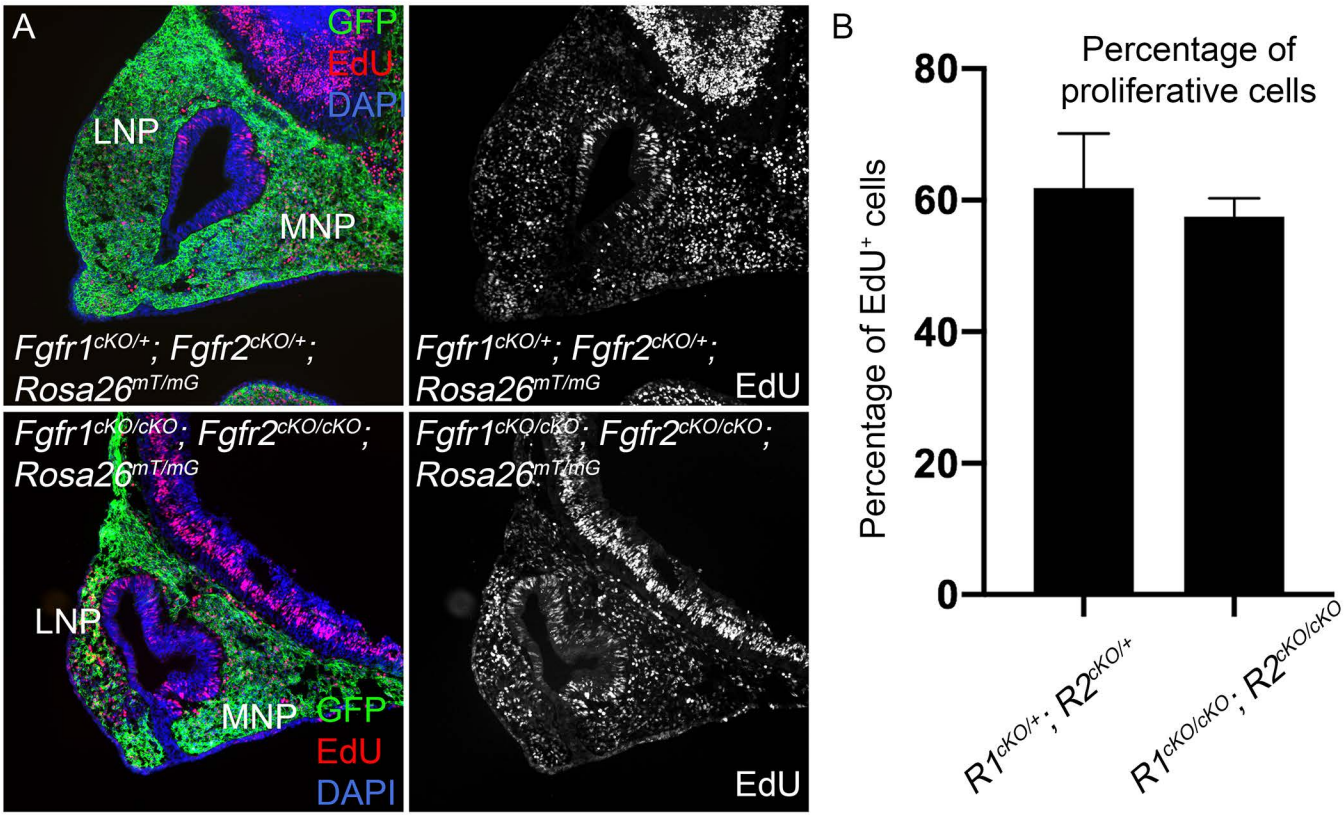

474 **Extended Data Fig. 3: Cell proliferation in *Fgfr1*$^{cKO/cKO}$; *Fgfr2*$^{cKO/cKO}$ double mutants.**

475 (A) EdU incorporation was used to assay cell proliferation in *Fgfr1*$^{cKO/cKO}$; *Fgfr2*$^{cKO/cKO}$;
476 *ROSA26*$^{mT/mG}$ double mutants. No change in the proliferation index of GFP^{+} cNCC lineage cells
477 was observed at E10.5 in the MNP and LNP across various genotypes.

478 (B) Quantification of the mean percentage of EdU^{+} cells normalized to GFP^{+} cNCC lineage
479 cells, in control versus double null mutant cells suggests cell proliferation remained unaffected in
480 *Fgfr1*$^{cKO/cKO}$; *Fgfr2*$^{cKO/cKO}$ double mutants.

481

482

Extended Data Figure 4

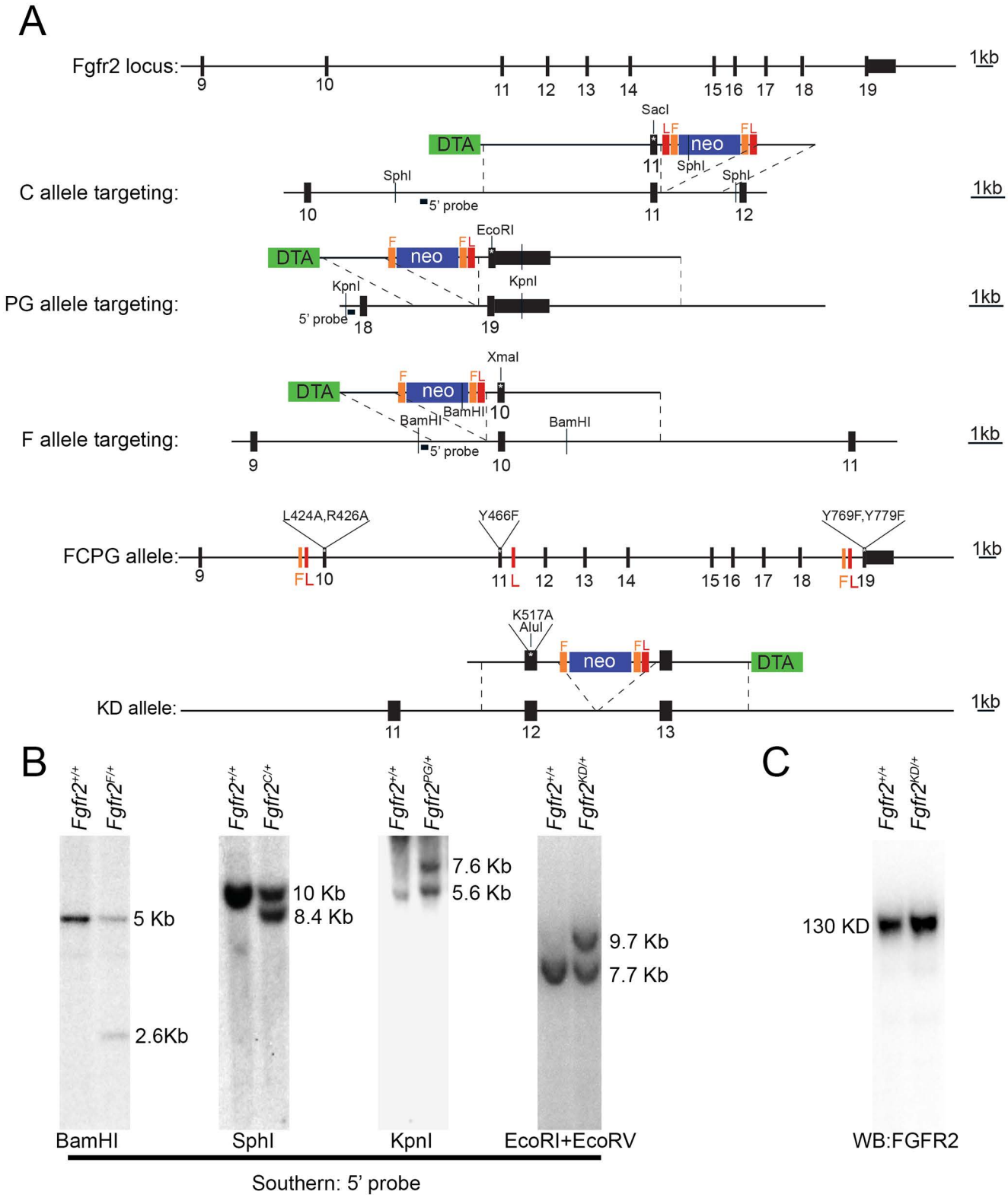

483 **Extended Data Fig. 4: Allelic series of *Fgfr2* signaling mutations.**

484 (A) Representation of *Fgfr2* WT locus, targeting vectors and the corresponding targeted loci
485 for C, PG and F alleles, the *Fgfr2*^{FCPG} locus, and the KD allele. Targeting vectors C, PG and F
486 introduced Y466F, Y769F/Y779F and L434A/R426A mutations sequentially to the *Fgfr2* locus,
487 respectively. The targeting vector for KD allele introduced the K517A mutation. ES cells were
488 targeted first with C targeting vector generating *Fgfr2*$^{+/C}$ mutant cells. *Fgfr2*$^{+/C}$ ES cells were
489 targeted with PG targeting vector generating either *Fgfr2*$^{C/PG}$ or *Fgfr2*$^{+/CPG}$ mutant cells. Finally,
490 *Fgfr2*$^{+/CPG}$ was targeted with F targeting vector resulting in *Fgfr2*$^{F/CPG}$ or *Fgfr2*$^{+/FCPG}$ mutant ES
491 cells. Multiple LoxP sites were introduced at the *Fgfr2* locus during successive rounds of targeting,
492 and the neo cassette was removed *in vivo* or in culture before generating signaling mouse mutants.
493 We were unable to perform a conditional mutation for the *Fgfr2*^{FCPG} allele due to the serial
494 retention of multiple lox sites during the generation of this allele. Abbreviation: L, loxP site; F, FRT
495 site; DTA, Diptheria toxin A cassette; Neo, Neomycin resistance cassette.

496 (B) Southern blot confirmation for proper targeting of F, C, PG and KD mutations at the *Fgfr2*
497 locus. 5' probes used for each targeting events are indicated. BamHI restriction enzyme
498 generated 5kb and 2.6kb band for WT and F targeted loci, respectively. SphI digestion generated
499 10kb and 8.4 kb fragment for WT and C targeted loci, respectively. KpnI digestion generated a
500 5.6kb band for WT locus and a 7.6kb band for PG targeted locus. EcoRI and EcoRV restriction
501 digestion generated 7.7kb WT fragment and 9.7kb KD-mutant fragment.

502 (C) Western blot from facial prominence cells harvested from E9.5 wild-type and *Fgfr2*$^{KD/KD}$
503 embryos show full length FGFR2^{KD} protein expression.

504

505

Extended Data Figure 5

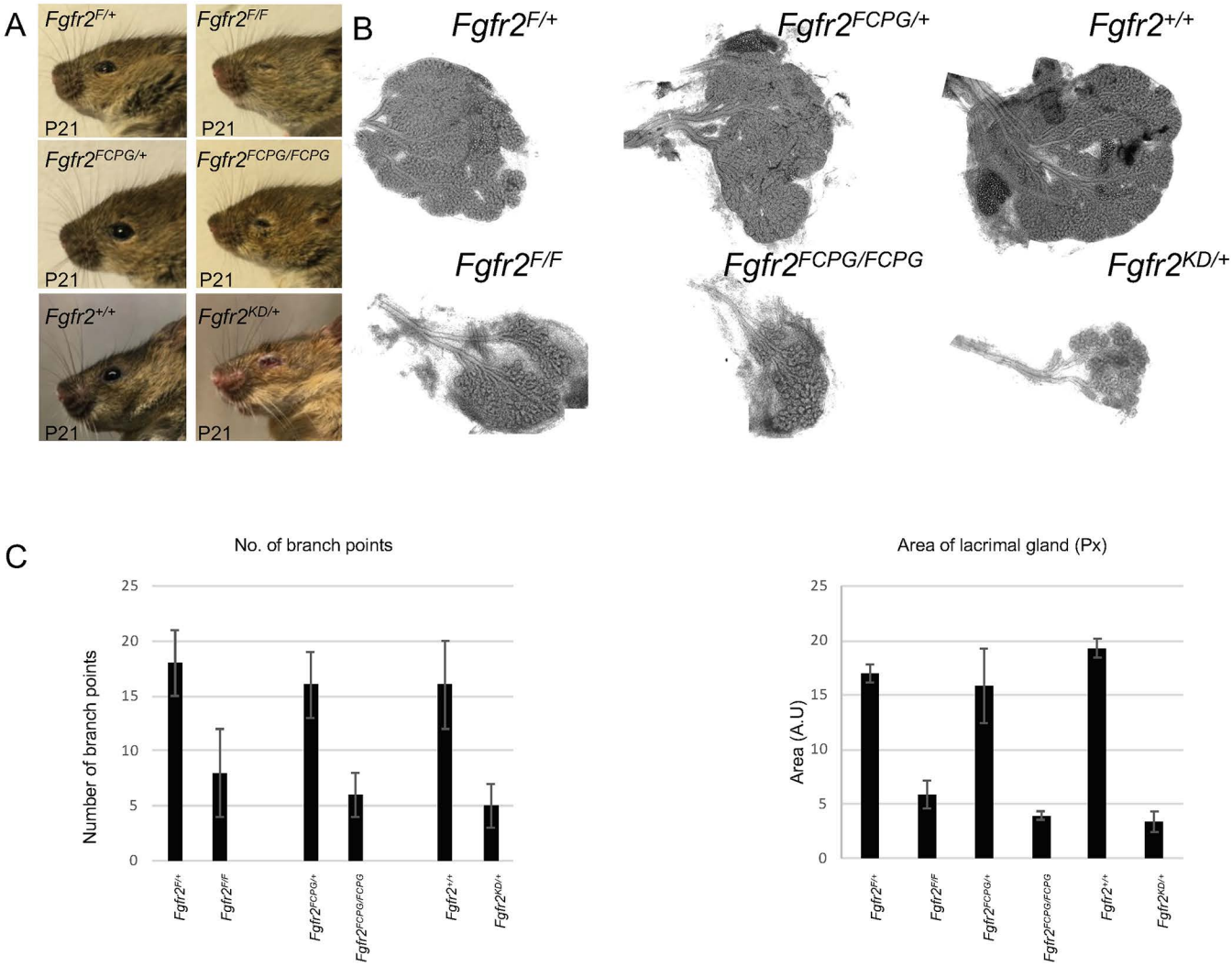

506 **Extended Data Fig. 5: Lacrimal gland defects in *Fgfr2* signaling mutants.**

507 (A) Sagittal view of the left eye at P21 for the mentioned genotypes. *Fgfr2*$^{F/F}$, *Fgfr2*$^{FCPG/FCPG}$
508 and *Fgfr2*$^{KD/+}$ mice showed fully penetrant defects with onset at P15 which included laceration
509 around the eye. More severe defects were observed in *Fgfr2*$^{KD/+}$ mutants.

510 (B) The lacrimal gland from signaling mutants was dissected at P5 and stained with
511 acetocarmine. Representative images are shown here for *Fgfr2*$^{F/F}$, *Fgfr2*$^{FCPG/FCPG}$ and *Fgfr2*$^{KD/+}$
512 compared to littermate *Fgfr2*$^{F/+}$, *Fgfr2*$^{FCPG/+}$ and *Fgfr2*$^{+/+}$ controls.

513 (C) Acetocarmine stained preparation of exorbital lacrimal glands at P5 from *Fgfr2*$^{F/F}$,
514 *Fgfr2*$^{FCPG/FCPG}$ and *Fgfr2*$^{KD/+}$ mice showed reduced branching and reduced overall size of the gland.
515 Flat mounts of the acetocarmine stained lacrimal glands for each genotype were microscopically
516 analyzed and primary and secondary branching points were counted manually. The bar graph
517 shows the mean ± standard deviation of the relative number of branch points for each genotype
518 analyzed. The relative size of the lacrimal gland for each genotype was also assessed by
519 comparing images acquired in the same magnification as a mean of the area observed in flat
520 mounts. *Fgfr2*$^{F/F}$, *Fgfr2*$^{FCPG/FCPG}$ and *Fgfr2*$^{KD/+}$ compared to littermate *Fgfr2*$^{F/+}$, *Fgfr2*$^{FCPG/+}$ and
521 *Fgfr2*$^{+/+}$controls show reduced branching and a reduction in the overall size of the gland.

522

523

Extended Data Figure 6

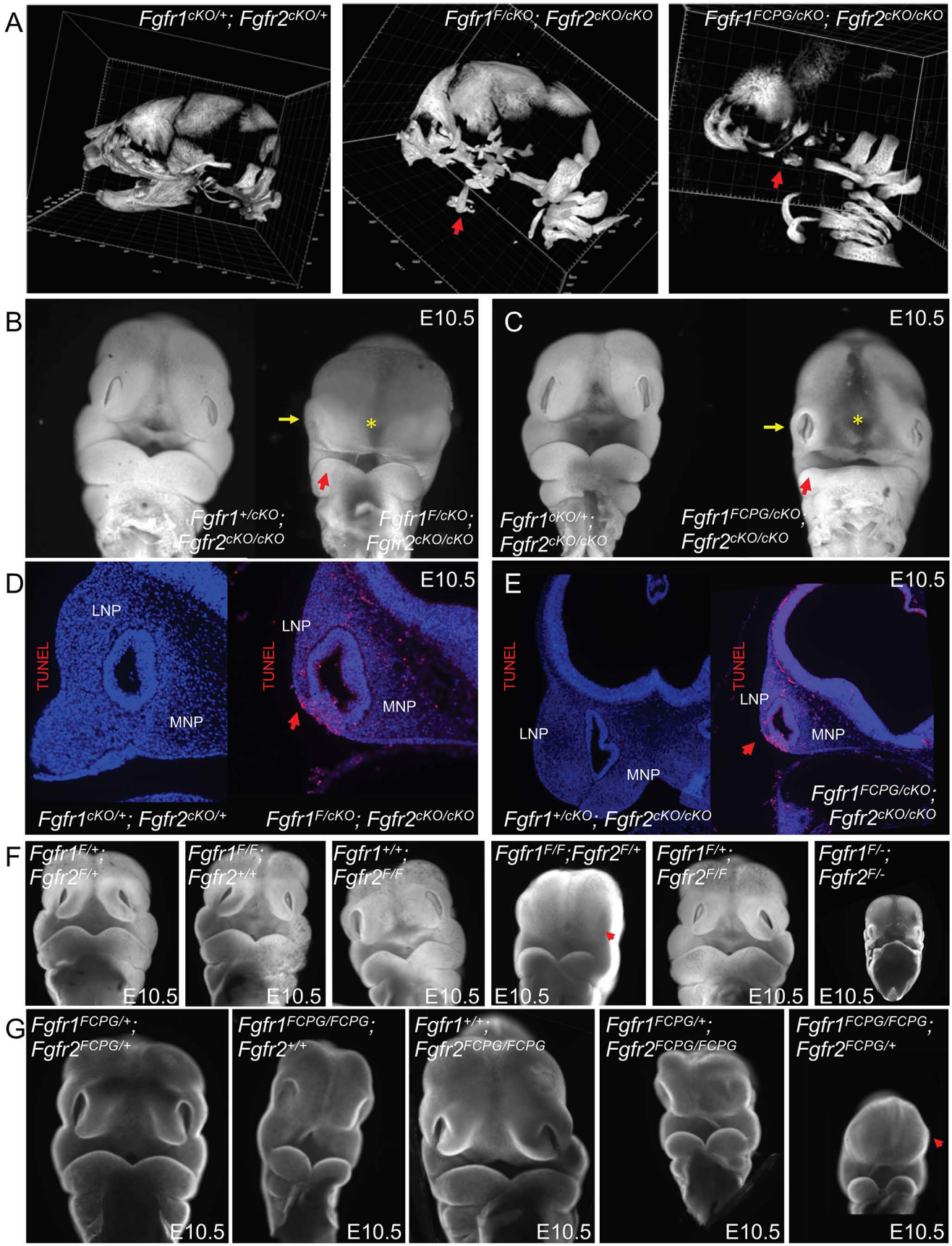

524 **Extended Data Fig. 6: Analysis of *Fgfr1* and *Fgfr2* single and compound signaling mutants.**
525 (A) Micro-CT analysis of control *Fgfr1*$^{cKO/+}$; *Fgfr2*$^{cKO/+}$ embryos at E18.5 compared to *Fgfr1*$^{F/cKO}$;
526 *Fgfr2*$^{cKO/+}$ and *Fgfr1*$^{FCPG/cKO}$; *Fgfr2*$^{cKO/+}$ embryos at similar stages. The mandible (red arrow) was
527 more severely affected in *Fgfr1*$^{FCPG/cKO}$; *Fgfr2*$^{cKO/+}$ than in *Fgfr1*$^{F/cKO}$; *Fgfr2*$^{cKO/+}$ embryos.
528 (B) Frontal facial view of DAPI-stained E10.5 *Fgfr1*$^{F/cKO}$; *Fgfr2*$^{cKO/+}$ embryos compared to
529 control *Fgfr1*$^{cKO/+}$; *Fgfr2*$^{cKO/+}$ embryos. Midline separation (yellow asterisk) was observed and facial
530 prominences were hypoplastic (yellow arrow), however, no defect in the mandible (red arrow) was
531 observed.
532 (C) Frontal facial view of DAPI-stained E10.5 *Fgfr1*$^{FCPG/cKO}$; *Fgfr2*$^{cKO/+}$ embryos compared to
533 control *Fgfr1*$^{cKO/+}$; *Fgfr2*$^{cKO/+}$ embryos. In the mutants, midline separation (yellow asterisk) and
534 facial prominence (yellow arrow) defects were more severe than *Fgfr1*$^{F/cKO}$; *Fgfr2*$^{cKO/+}$ embryos. A
535 defect in the mandible (red arrow) was also more severe than *Fgfr1*$^{F/cKO}$; *Fgfr2*$^{cKO/+}$ embryos.
536 (D-E) Cell-death analysis by TUNEL staining in the facial prominences of (D) *Fgfr1*$^{F/cKO}$;
537 *Fgfr2*$^{cKO/+}$ and (E) *Fgfr1*$^{FCPG/cKO}$; *Fgfr2*$^{cKO/+}$ embryos at E10.5, showing multiple dying cells in both
538 the MNP and the LNP compared to the *Fgfr1*$^{cKO/+}$; *Fgfr2*$^{cKO/+}$ controls.
539 (F) Frontal facial view of DAPI-stained *Fgfr1*^{F} and *Fgfr2*^{F} compound mutant embryos at E10.5.
540 *Fgfr1*$^{F/F}$; *Fgfr2*$^{+/F}$ embryos had defects in the development of facial prominences, as opposed to
541 *Fgfr1*$^{F/+}$; *Fgfr2*$^{F/+}$ controls. Mandibular prominences were hypoplastic, however, the maxillary
542 prominences, FNP and MNP were more severely affected. *Fgfr1*$^{F/F}$; *Fgfr2*$^{+/+}$ mutants, *Fgfr1*$^{+/+}$;
543 *Fgfr2*$^{F/F}$ mutants, and *Fgfr1*$^{F/+}$; *Fgfr2*$^{F/F}$ mutants did not show obvious defects at this stage. *Fgfr1*$^{F/F}$;
544 *Fgfr2*$^{+/F}$ mutant embryos were also developmentally retarded. We did not recover *Fgfr1*$^{F/F}$; *Fgfr2*$^{F/F}$
545 mutant embryos by E9.5.
546 (G) The craniofacial phenotype at E10.5 of DAPI-stained *Fgfr1*^{FCPG} and *Fgfr2*^{FCPG} compound
547 mutant embryos. We observed the posterior truncation for *Fgfr1*$^{FCPG/FCPG}$ mutant embryos. The
548 introduction of one copy of *Fgfr2*^{FCPG} allele on a *Fgfr1*$^{FCPG/FCPG}$ background resulted in severe
549 growth retardation of the facial prominences compared to control *Fgfr1*$^{+/FCPG}$; *Fgfr2*$^{FCPG/FCPG}$
550 embryos. *Fgfr2*$^{FCPG/FCPG}$ and *Fgfr1*$^{+/FCPG}$; *Fgfr2*$^{FCPG/FCPG}$ embryos did not exhibit abnormal
551 phenotypes and were comparable to WT embryos.
552
553

Extended Data Figure 7

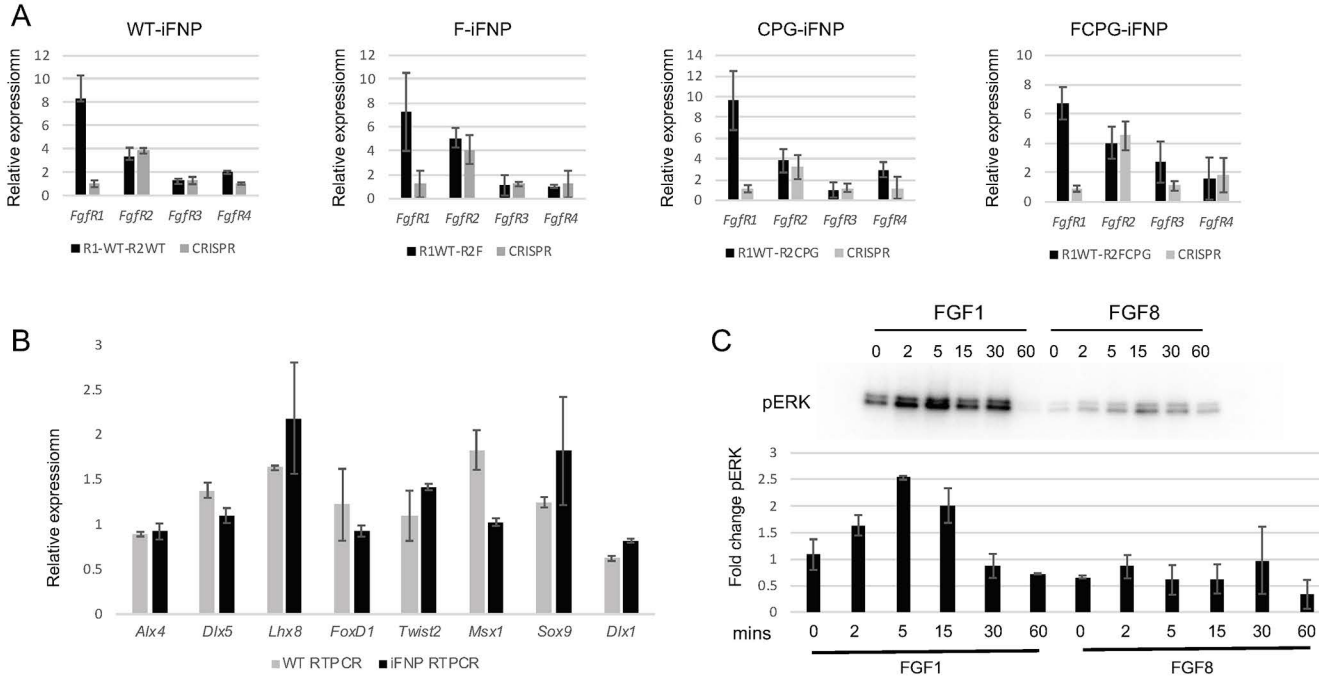

554 **Extended Data Fig. 7: Characterization of *Fgfr1 null* mutant iFNP cells.**

555 (A) *Fgfr1, Fgfr3, Fgfr4* and *Fgfr2*^{WT} mRNA expression in wild-type and *Fgfr2*^{F}, *Fgfr2*^{CPG} and
556 *Fgfr2*^{FCPG} iFNP cells before and after *Fgfr1*-CRISPR disruption, as determined by RT-qPCR.

557 (B) *Alx4, Dlx1, Dlx5, FoxD1, Twist1* and *Lhx8* were all expressed at similar levels by
558 quantitative real-time PCR (qRT-PCR) in both immortalized FNP (iFNP) cells and primary FNP
559 cells derived from wild-type embryos. Only *Msx1* expression was 1.8-fold higher in wild-type
560 primary FNP cells compared to iFNP cell lines. These results identify iFNP cells as a suitable cell
561 type to interrogate FGF signaling functions in craniofacial development.

562 (C) *WT*-iFNP cells were serum starved overnight and stimulated with either 50 ng/mL FGF1
563 or 50 ng/mL FGF8-b and 5 µg/mL heparin for the indicated times (0-60 mins). Robust ERK1/2
564 activation was observed with FGF1 treatment compared to FGF8-b treatment.

565

566

Extended Data Figure 8

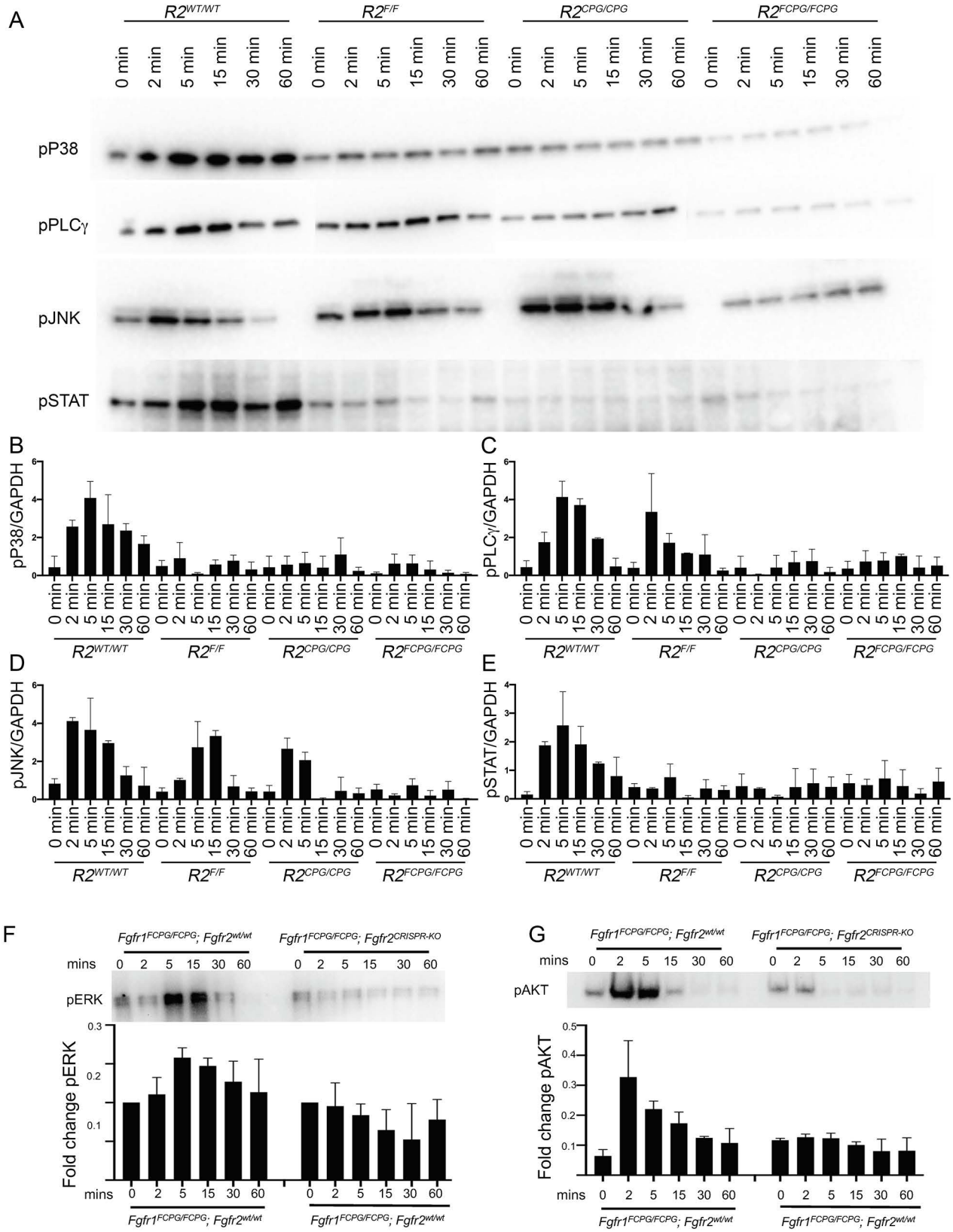

567 **Extended Data Fig. 8: Intracellular signaling upon FGF1 stimulation.**

568 (A) iFNP cells derived from the indicated genotypes, *Fgfr2*$^{wt/wt}$ (*R2*$^{wt/w}$), *Fgfr2*$^{F/F}$ (*R2*$^{F/F}$),
569 *Fgfr2*$^{CPG/CPG}$ (*R2*$^{CPG/CPG}$) and *Fgfr2*$^{FCPG/FCPG}$ (*R2*$^{FCPG/FCPG}$), were serum starved overnight and
570 stimulated with 50 ng/mL FGF1 and 5 µg/mL heparin for the indicated times (0-60 mins).
571 Phospho-blots were stripped and reblotted with GAPDH as a loading control. Activation of pP38,
572 pPLCγ, pJNK and pSTAT3 was investigated.

573 (B-E) Quantification of pathway activation for (B) pP38, (C) pPLCγ, (D) pJNK and (E) pSTAT3
574 normalized to the GAPDH loading control, is reported as mean ± standard deviation with a
575 minimum of three independent biological replicates.

576 (F-G) *Fgfr1*^{FCPG} *Fgfr2* null iFNP (*Fgfr1*^{FCPG}*; Fgfr2*$^{CRISPR-KO}$) cells generated using CRISPR/Cas9.
577 Upon FGF1 stimulation, we observed peak activation of (F) pERK1/2 after 2 mins in *Fgfr1*$^{FCPG/FCPG}$
578 iFNP cells. We did not observe activation over background in *Fgfr1*$^{FCPG/FCPG}$; *Fgfr2*$^{CRISPR-KO}$ iFNP
579 cells. (G) pAKT activation was undetectable in both *Fgfr1*$^{FCPG/FCPG}$; *Fgfr2*$^{CRISPR-KO}$ in contrast to
580 *Fgfr1* $^{FCPG/FCPG}$*; Fgfr2*$^{+/+}$ iFNP cells.

581

582

Extended Data Figure 9

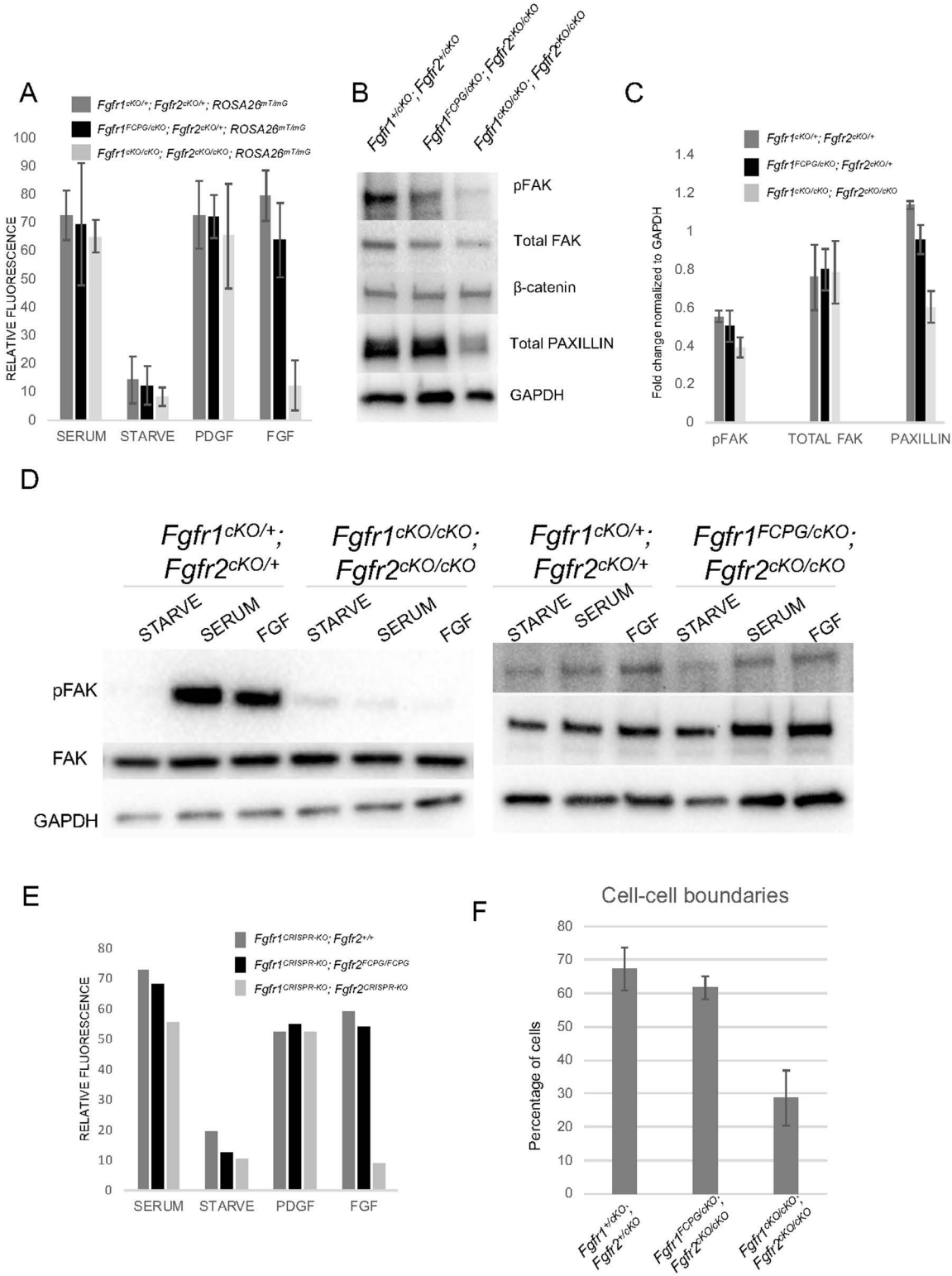

583 **Extended Data Fig. 9: FGFR signaling in cell-matrix and cell-cell adhesion.**

584 (A) Quantification of Paxillin immunostaining mean fluorescence intensity in FNP cells, shown
585 for different genotypes in Fig. 4B. Mean fluorescence intensity in starvation media act as a
586 baseline. Upon serum stimulation or PDGF treatment, cells from all genotypes showed a robust
587 increase in focal adhesions. Upon FGF treatment, control cells and *Fgfr1*$^{FCPG/cKO}$*; Fgfr2*$^{cKO/+}$*;*
588 *ROSA26*$^{mT/mG}$ FNP cells showed robust paxillin accumulation, in contrast to *Fgfr1*$^{cKO/cKO}$*;*
589 *Fgfr2*$^{cKO/cKO}$*; ROSA26*$^{mT/mG}$ double mutant cells.

590 (B) Western Blot analysis of freshly harvested FNP cells from control, *Fgfr1*$^{FCPG/cKO}$*; Fgfr2*$^{cKO/+}$*;*
591 *ROSA26*$^{mT/mG}$ and *Fgfr1*$^{cKO/cKO}$*; Fgfr2*$^{cKO/cKO}$*; ROSA26*$^{mT/mG}$ double mutant FNP cells for pFAK, total
592 FAK, β-catenin and Paxillin. GAPDH was used as a loading control. Total FAK and β-catenin
593 levels remained constant across all genotypes.

594 (C) Bar graph shows relative levels of pFAK, total FAK and Paxillin. pFAK and Paxillin levels
595 were comparable in control and *Fgfr1*$^{FCPG/cKO}$*; Fgfr2*$^{cKO/+}$*; ROSA26*$^{mT/mG}$ FNP cells, but severely
596 reduced in *Fgfr1*$^{cKO/cKO}$*; Fgfr2*$^{cKO/cKO}$*; ROSA26*$^{mT/mG}$ FNPs. Total FAK levels remained unchanged.

597 (D) Freshly harvested *Fgfr1*$^{cKO/+}$*; Fgfr2*$^{cKO/+}$*; ROSA26*$^{mT/mG}$ control, *Fgfr1*$^{FCPG/cKO}$*; Fgfr2*$^{cKO/+}$*;*
598 *ROSA26*$^{mT/mG}$, and *Fgfr1*$^{cKO/cKO}$*; Fgfr2*$^{cKO/cKO}$*; ROSA26*$^{mT/mG}$ double mutant FNP cells were treated
599 with serum or FGF1 for 15 mins, before assessing levels of pFAK by western blot. *Fgfr1*$^{cKO/+}$*;*
600 *Fgfr2*$^{cKO/+}$*; ROSA26*$^{mT/mG}$ control and *Fgfr1*$^{FCPG/cKO}$*; Fgfr2*$^{cKO/+}$*; ROSA26*$^{mT/mG}$ FNP cells showed a
601 comparable increase in FAK activation upon FGF stimulation. In contrast, *Fgfr1*$^{cKO/cKO}$*; Fgfr2*$^{cKO/cKO}$*;*
602 *ROSA26*$^{mT/mG}$ double mutant FNP cells failed to activate FAK in both serum-stimulated and FGF
603 treated conditions.

604 (E) Quantification of mean fluorescence from Paxillin immunostaining in *Fgfr2*$^{WT/WT}$
605 (*Fgfr1*$^{CRISPR-KO}$ *Fgfr2*$^{WT/WT}$), *Fgfr2*$^{FCPG/FCPG}$ (*Fgfr1*$^{CRISPR-KO}$ *Fgfr2*$^{FCPG/FCPG}$), and *Fgfr2*$^{-/-}$ (*Fgfr1*$^{CRISPR-}$
606 ^{KO} *Fgfr2* $^{CRISPR-KO}$) -iFNP cells upon serum starvation and growth factor treatments shown in Fig.
607 4B. Upon serum stimulation or PDGF treatment, cells from all genotypes showed a robust
608 increase in focal adhesions. Upon FGF treatment, both control and *Fgfr1*$^{CRISPR-KO}$ *Fgfr2*$^{FCPG/FCPG}$
609 iFNP cells showed robust paxillin accumulation at focal adhesions, whereas *Fgfr1*$^{CRISPR-KO}$ *Fgfr2*
610 $^{CRISPR-KO}$ double null mutant iFNP cells showed poor response.

611 (F) Quantification of percentage of cells that form cell boundaries (n=500 contacts for each
612 genotype) in *Fgfr1*$^{cKO/+}$*; Fgfr2*$^{cKO/+}$*; ROSA26*$^{mT/mG}$ control, *Fgfr1*$^{FCPG/cKO}$*; Fgfr2*$^{cKO/+}$*; ROSA26*$^{mT/mG}$,
613 and *Fgfr1*$^{cKO/cKO}$*; Fgfr2*$^{cKO/cKO}$*; ROSA26*$^{mT/mG}$ double mutant FNP cells. When freshly harvested
614 primary FNP cells were serum stimulated for 3 hrs, both control and *Fgfr1*$^{FCPG/cKO}$*; Fgfr2*$^{cKO/+}$*;*
615 *ROSA26*$^{mT/mG}$ cells formed comparable numbers of cell-cell contacts (Figure 7D). In contrast, this
616 number was reduced to half in double mutant FNP cells.

Supplementary Information Image S1

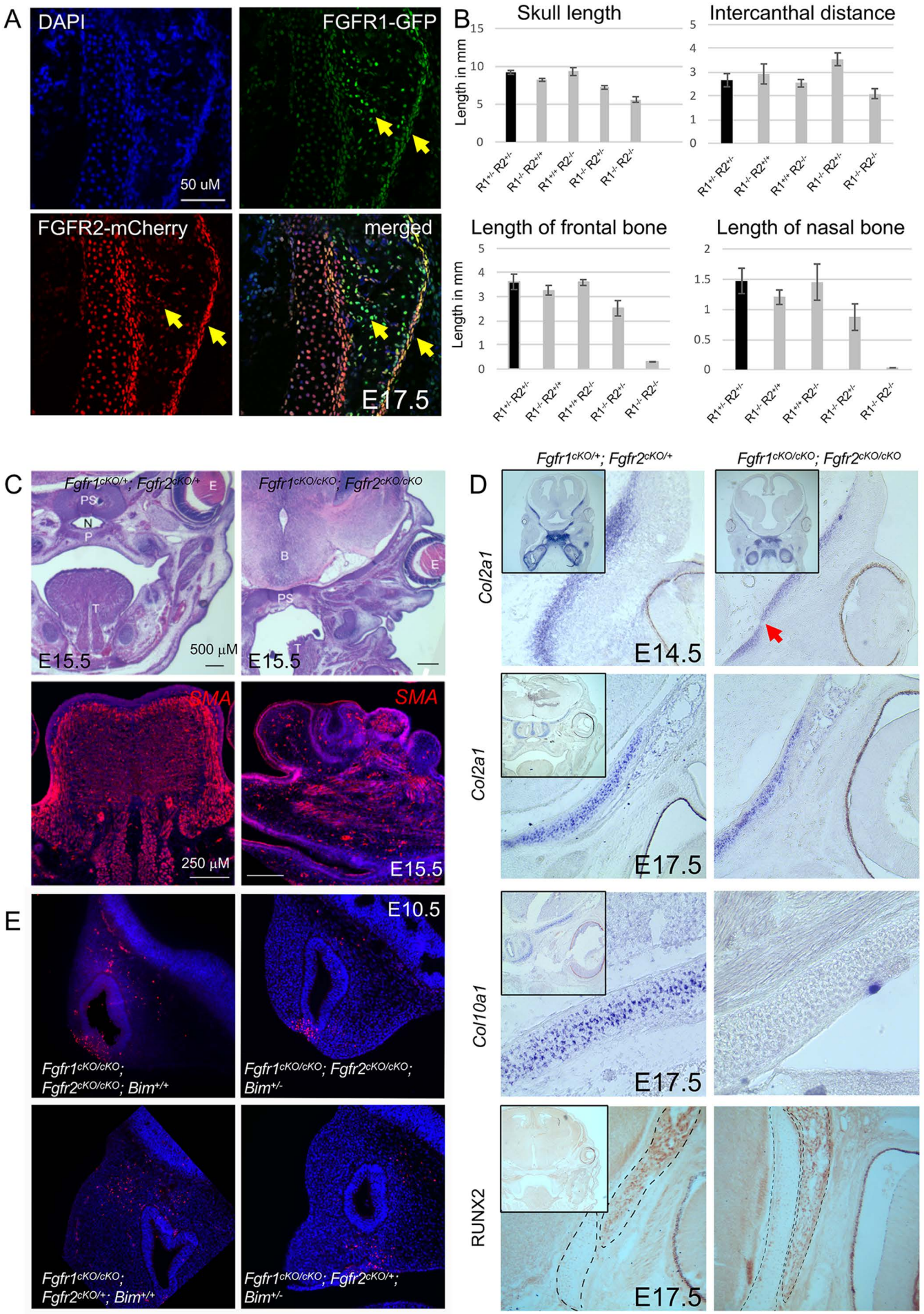

Supplementary Information Figure S1: Craniofacial ossification and organogenesis defects in *Fgfr1/2* mutants.

(A) Spatial domain of FGFR1 and FGFR2 expression in the frontal bone at E17.5. GFP and mCherry immunohistochemistry was used to detect expression from *Fgfr1-GFP* and *Fgfr2-mCherry* reporter alleles. Co-expression of both FGFR1-GFP and FGFR2-mCherry was observed in the cartilage and the perichondrium (yellow arrow).

(B) Quantification of skull length, intercanthal distance, length of frontal and nasal bone for different genotypes measured in millimeters (mm).

(C) Histological examination at E15.5 showed defective organogenesis in multiple organs, including the palate, tongue, and skeleton. In the double mutants several skeletal structures such as palate (P), nasopharyngeal lumen (N) and pre-sphenoid (PS) were affected compared to the controls. Non-neural crest derived muscles in the tongue were also affected. SMA immunofluorescence showed organized muscle fiber differentiation in controls. In the *Fgfr1/2* mutants, muscle fiber differentiation appeared random and disorganized.

(D) Differentiation of craniofacial skeleton was assessed by studying the expression of cartilage differentiation marker, *Col2a1,* on sections. mRNA *in situ* hybridization analysis at E14.5 showed *Col2a1* expression in the chondrocranium (skull base) and mandible in the control (inset shows low magnification view of the region). In the double mutants, however, expression was restricted to a narrow band of cells in the skull base. Expression of *Col2a1* and of *Col10a1* and Runx2 (mature cartilage markers) was assessed at E17.5 on sections (inset shows a low magnification view of the region). *Col2a1* mRNA expression was restricted to the skull base, mandible and frontal bone in controls. A similar expression was also observed in conditional double mutants. At E17.5, *Col10a1* mRNA expression was much broader in the controls. In conditional double mutants, *Col10a1* expression was undetectable suggesting a block in terminal chondrogenic differentiation. We detected the expression of mature cartilage and late osteoblast marker, RUNX2, in both controls and the conditional double mutants.

(E) Increased cell-death observed in conditional double mutants was partially rescued in *Fgfr1*$^{cKO/cKO}$*; Fgfr2*$^{cKO/cKO}$; *Bim*$^{+/-}$ mutants at E10.5. More TUNEL^{+} cells were observed in the LNP in *Fgfr1*$^{cKO/cKO}$*; Fgfr2*$^{cKO/cKO}$ and *Fgfr1*$^{cKO/cKO}$*; Fgfr2*$^{cKO/+}$ mutants compared to corresponding *Fgfr1*$^{cKO/cKO}$*; Fgfr2*$^{cKO/cKO}$*; Bim*$^{+/-}$ and *Fgfr1*$^{cKO/cKO}$*; Fgfr2*$^{cKO/+}$; *Bim*$^{+/-}$ counterparts. Compared to controls, reduced TUNEL positive foci were observed in *Fgfr1*$^{cKO/cKO}$*; Fgfr2*$^{cKO/cKO}$; *Bim*$^{+/-}$ mutants.

Supplementary Information Image S2

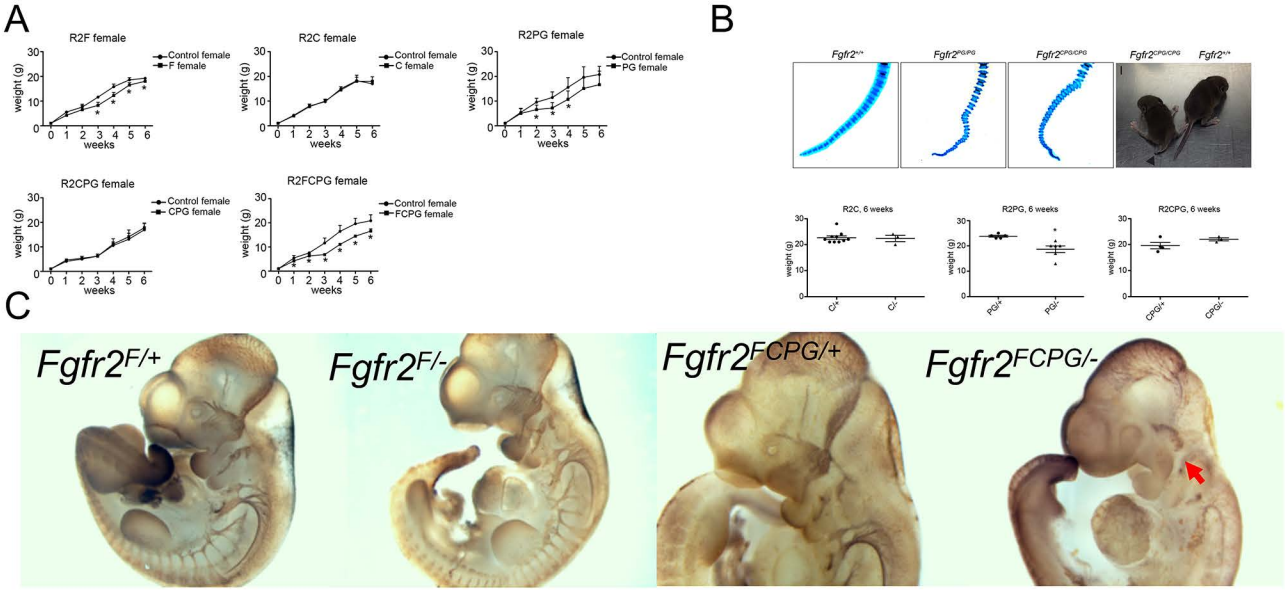

650 **Supplementary Information Figure S2: Growth defects in *Fgfr* signaling mutants.**

651 (A) Growth rate (in terms of weight gain) of homozygous *Fgfr2*$^{F/F}$, *Fgfr2*$^{C/C}$, *Fgfr2*$^{PG/PG}$,
652 *Fgfr2*$^{CPG/CPG}$, and *Fgfr2*$^{FCPG/FCPG}$ female versus control until 6 weeks shown as mean ± SEM. *
653 indicates p-value <0.05. We noted a decrease in growth rate for *Fgfr2*$^{F/F}$, *Fgfr2*$^{PG/PG}$, and
654 *Fgfr2*$^{FCPG/FCPG}$ mutant mice compared to control.

655 (B) *Fgfr2*$^{PG/PG}$ and *Fgfr2*$^{CPG/CPG}$ skeletal preparation at P0 showed fusion of the caudal
656 vertebrae, resulting in a kinked or curly tail phenotype in rare cases (black arrow). Hemizygote
657 *Fgfr2*$^{C/-}$, *Fgfr2*$^{PG/-}$ and *Fgfr2*$^{CPG/-}$ mice were weighed at 6 weeks. *Fgfr2*$^{PG/-}$ were smaller than their
658 control littermate.

659 (C) Whole mount immunohistochemistry for neurofilament staining revealed trigeminal nerve
660 defects at E10.5 in *Fgfr2*$^{FCPG/-}$ embryo but not in *Fgfr2*$^{F/-}$. In *Fgfr2*$^{F/+}$, *Fgfr2*$^{FCPG/+}$ and *Fgfr2*$^{F/-}$
661 embryos, trigeminal nerve migrated to the anterior domain of the PA1 (red arrow) at E10.5.
662 Trigeminal nerves fail to migrate into the pharyngeal arch of *Fgfr2*$^{FCPG/-}$ mutants.

663

Supplementary Information Table 1: Recovery of *Fgfr2* homozygous and *Fgfr2* hemizygous signaling mutants.

Recovery of *Fgfr2* signaling mutants			
P4-P10	Total	*/*	Recovery
$R2^{F}$	386	85	22%
$R2^{C}$	505	131	26%
$R2^{PG}$	475	78	16%
$R2^{CPG}$	396	70	18%
$R2^{FCPG}$	646	102	16%
$R2^{KD}$	38	0	0
E18.5	Total	*/*	Recovery
$R2^{F}$	97	22	23%
$R2^{C}$	53	14	26%
$R2^{PG}$	64	14	22%
$R2^{CPG}$	42	10	24%
$R2^{FCPG}$	87	22	25%
$R2^{KD}$	45	0	-
Recovery of *Fgfr2* hemizygous signaling mutants			
P4-P10	Total	*/-	Recovery
$R2^{F}$	37	0	-
$R2^{C}$	52	10	19%
$R2^{PG}$	47	13	27%
$R2^{CPG}$	53	12	22%
$R2^{FCPG}$	28	1	3%
P0-P1	Total	Observed	Expected
$R2^{F}$	33	4	12%
$R2^{FCPG}$	25	2	8%
E18.5	Total	Observed	Expected
$R2^{F}$	33	5	15%
$R2^{FCPG}$	31	10	32%

Fgfr2 signaling mutant heterozygotes ($Fgfr2^{F/+}$, $Fgfr2^{C/+}$, $Fgfr2^{PG/+}$, $Fgfr2^{CPG/+}$, $Fgfr2^{FCPG/+}$ and $Fgfr2^{KD/+}$) were intercrossed. Embryos were analyzed either at E18.5 or postnatally between P4 and P10. To identify *in vivo* phenotypes associated with *Fgfr2* signaling mutations, *Fgfr2* signaling mutant heterozygotes were crossed with $Fgfr2^{+/-}$ null heterozygotes. $Fgfr2^{C/-}$, $Fgfr2^{PG/-}$ and $Fgfr2^{CPG/-}$ embryos were analyzed at E18.5 and postnatally at P0 and between P4 and P10. Hemizygous $Fgfr2^{F/-}$ and $Fgfr2^{FCPG/-}$ mutant mice were recovered at expected Mendelian ratios at E18.5, but died postnatally.

Supplementary Information Table 2: Craniofacial structures differentially affected in conditional signaling mutants.

C/CPG<F<FCPG	***C/CPG<F=FCPG***
Nasal Cartilage	
Mandible	
Squamosal	
Maxilla	
	Premaxilla
	Frontal bone
	Zygomatic bone
	Tympanic bulla
	Basisphenoid
	Internal pterygoid process

Micro-CT examination of *Fgfr1*$^{F/cKO}$*; Fgfr2*$^{cKO/cKO}$ and *Fgfr1*$^{FCPG/cKO}$*; Fgfr2*$^{cKO/cKO}$ mutant mice skull were to *Fgfr1*$^{cKO/cKO}$*; Fgfr2*$^{cKO/cKO}$ mutants at E18.5. *Fgfr1*$^{FCPG/cKO}$*; Fgfr2*$^{cKO/cKO}$ mutant skull show a more severe defect than *Fgfr1*$^{F/cKO}$*; Fgfr2*$^{cKO/cKO}$ mutants. Several structures are differentially affected in *Fgfr1*$^{F/cKO}$*; Fgfr2*$^{cKO/cKO}$ and *Fgfr1*$^{FCPG/cKO}$*; Fgfr2*$^{cKO/cKO}$ mutants. Most severe defects are observed in *Fgfr1*$^{cKO/cKO}$*; Fgfr2*$^{cKO/cKO}$ mutants.

720 **Supplementary Information Table S3: Homology arms used in targeting vectors.**

	Short homology arm (corresponding primer binding region)	Notes	Long homology arm (corresponding primer binding region)	Notes
Fgfr2^{F}	GCTCTTTCTCTCTATGGGTT and ATTCGACTGTAATGGGGGAC	1.7kb region between exon 9-10	TGGTATCAGCTGCTCACTGG and GCCCACCCTGAATAACCATG	5.1kb spanning exon10
Fgfr2^{C}	CTTTCTGCATCAAAGACACA and GGTTACATCGATTGCCCAGT	1.7kb region between exon 11-12	GGCCACAATTCAGAGGGAAG and AGCCCATTTTTCCACCTTCT	5.1kb spanning exon11
Fgfr2^{PG}	TCTTGGCTGTGGCTTGTACTGG and AGGACCTCGGTGACCCACTA	1.9kb region between exon 18-19	GTAGCAGAGTGGGCAAGCTC and AGGAACTGCAAGAGGACCAA	5.4kb spanning exon19 and 3'-UTR
Fgfr2^{KD}	GGTACCCAAGTGTGGAAAAT and GTTTGCTCCTTTTTGGCTTC	SmaI to MfeI, 1.9kb spanning exon12	GAACTGATGCAGAATCCCAG and CCATTVTAAGTCCCTTGAGC	MfeI to BclI 3.7kb spanning exon13

721

722 **Supplementary Information Table S4: Nucleotide and amino-acid substitutions in signaling**
723 **mutations for *Fgfr2.***

Mutation	Nucleotide substitution	Amino acid substitution	Notes
F	CTG to GCC AGA to GCA	L424A R426A	Introduces an XmaI site
C	TAT to TTT TTG to CTC	Y466F L468L	Introduces a SacI site
PG	TAC to TTC TAT to TTT	Y769F Y779F	Introduces an EcoRI site
KD	GAAG to AGCT	K517A	Introduces an AluI site

724

725 **Supplementary Information Table S5: List of oligonucleotides used in this study.**

726

Gene	Forward	Purpose
Fgfr2^{F} 5' probe F	ACACTGGAGGATGGTGAAGG	Probes for Southern blot
Fgfr2^{F} 5' probe R	GACATGCATGCAATTGAACA	Probes for Southern blot
Fgfr2^{F} 3' probe F	GTCCCAGCTCAGCAATAAGC	Probes for Southern blot
Fgfr2^{F} 3' probe R	AGTGGTCACCTTCGGAGAGA	Probes for Southern blot
Fgfr2^{C} 5' probe F	GTGGGACAGCCTGGTAGGTA	Probes for Southern blot
Fgfr2^{C} 5' probe R	CGGGTAGGCTATGCACTCAT	Probes for Southern blot
Fgfr2^{C} 3' probe F	ATACTTGACCTGGCGGTTGA	Probes for Southern blot
Fgfr2^{C} 3' probe R	GGCATTTATAGCGTGGCATT	Probes for Southern blot
Fgfr2^{PG} 5' probe F	GTGTGAATGCTGCTTGTGCT	Probes for Southern blot
Fgfr2^{PG} 5' probe R	GCGGAAGCCTTGTTTTATGA	Probes for Southern blot
Fgfr2^{PG} 3' probe F	GGCCACGGAGTAGTTCAGAG	Probes for Southern blot
Fgfr2^{PG} 3' probe R	GCAAGCACATTTGTTTACCTG	Probes for Southern blot
Fgfr2^{KD} 5' probe F	TGGGTATGGCCAGCTCTAGT	Probes for Southern blot
Fgfr2^{KD} 5' probe R	TGCACACGAACCCAGCTATT	Probes for Southern blot
Fgfr2^{KD} 3' probe F	ATCCGTGCCTTTCTGAGTGG	Probes for Southern blot
Fgfr2^{KD} 3' probe R	TGCCAGCCATTTACCTCAGG	Probes for Southern blot
Fgfr2^{C}Forward-Genotyping	GTAAGTACTCTCCCTCTGGG	Genotyping
Fgfr2^{C}Reverse-Genotyping	AGCTGGCCATACCCAGACTTG	Genotyping
Fgfr2^{PG}Forward-Genotyping	CTGTTGCTTACTCTGGAGCT	Genotyping
Fgfr2^{PG}Reverse-Genotyping	GATACCCCAACTCCATTCAC	Genotyping
Fgfr2^{F}Forward-Genotyping	GGACCATATGAAGGGACTTG	Genotyping
Fgfr2^{F}Reverse-Genotyping	CTCGGTTTATCACTACAGCC	Genotyping
Fgfr2^{KD}Forward-Genotyping	ATAGCCTGCGTGTGTATCGG	Genotyping*
Fgfr2^{KD}Reverse-Genotyping	CGTCCCTGCAGAGTTCACAT	Genotyping*
Alx4-forward	ACACATGGGCAGCCTGTTTG	RT-PCR
Alx4-reverse	TGCTTGAGGTCTTGCGGTCT	RT-PCR
Gapdh-forward	AGGTCGGTGTGAACGGATTTG	RT-PCR
Gapdh-reverse	TGTAGACCATGTAGTTGAGGTCA	RT-PCR
Dlx5-forward	CAGAAGAGTCCCAAGCATCC	RT-PCR
Dlx5-reverse	GGTGACTGTGGCGAGTTA	RT-PCR

Lhx8-forward	ATGTATTGGAAGAGCGATCAG	RT-PCR
Lhx8-reverse	TCATTGGATGGGGTAACAAGGGC	RT-PCR
FoxD1-forward	TGAGCACTGAGATGTCCGATG	RT-PCR
FoxD1-reverse	CACCACGTCGATGTCTGTTTC	RT-PCR
Twist2-forward	AGCGCCCAGAGCTTCGAGGA	RT-PCR
Twist2-reverse	CGGCGAAGGCCTCGTTCAGG	RT-PCR
Msx1-forward	TCTCGGCCATTTCTCAGTCG	RT-PCR
Msx1-reverse	AGAGCATCTTCTGGCAGCTTG	RT-PCR
Sox9-forward	AGGAAGTCGGTGAAGAACGG	RT-PCR
Sox9-reverse	TGGAAGGTGAATTTCTCTGGG	RT-PCR
Dlx1-forward	TGGAATCCGAACTCCTCATC	RT-PCR
Dlx1-reverse	TGCTGCATAGCTTCTTGGTG	RT-PCR
Fgfr1-forward	CACATCGAGGTGAACGGGAGTAAG	RT-PCR
Fgfr1-reverse	CGCATCCTCAAAGGAGACATTCC	RT-PCR
Fgfr2-forward	GATGTGGAGTTTGTCTGCAAGGTTT	RT-PCR
Fgfr2-reverse	GACTGGTTGGCCTGCCCTATATAAT	RT-PCR
Fgfr3-forward	TGCGGTGCCTTCACAGA	RT-PCR
Fgfr3-reverse	ACTTGGACCTCTCCGTG	RT-PCR
Fgfr4-forward	GTACCCTCGGACCGCGGCACATAC	RT-PCR
Fgfr4-reverse	GCCGAAGCTGCTGCCGTTGATG	RT-PCR
Fgfr1-Ex6 -Crispr	CACCGCTGTTAGCCACACAAAGCAC	CRISPR Fgfr1
Fgfr1-Ex6 -Crispr	AAACGTGCTTTGTGTGGCTAACAGc	CRISPR Fgfr1
Fgfr1-Ex6 -Crispr	CACCGAAGAAGGAAGAAGGGGGAGG	CRISPR Fgfr1
Fgfr1-Ex6 -Crispr	AAACCCTCCCCCTTCTTCCTTCTTc	CRISPR Fgfr1
Fgfr2-Ex5 -Crispr	CACCGCTTCCTGGGCATTTGAACCC	CRISPR Fgfr2
Fgfr2-Ex5 -Crispr	AAACGGGTTCAAATGCCCAGGAAGc	CRISPR Fgfr2
Fgfr2-Ex5 -Crispr	CACCGCCATAAGATGTCATCTGAGA	CRISPR Fgfr2
Fgfr2-Ex5 -Crispr	AAACTCTCAGATGACATCTTATGGc	CRISPR Fgfr2
Fgfr1-CRISPR-Screen	TGCAGGAAGGATTCTGAGTGT	Screening Fgfr1 CRISPR clones
Fgfr1-CRISPR-Screen	GCTGTCTGGGCTAAAGTCTG	Screening Fgfr1 CRISPR clones
Fgfr2-CRISPR-Screen	CCCAAGCCCATAAAACCTGG	Screening Fgfr2 CRISPR clones

Fgfr2-CRISPR-Screen	CAAGGACACACGTTCACAGG	Screening Fgfr2 CRISPR clones

727 * Note: Genotyping *Fgfr2*^{KD} is followed by AluI digestion after PCR (Supplementary Information
728 Table S6)
729

730 **Supplementary Information Table S6: Genotyping reactions to identify *Fgfr2* signaling**
731 **mutations.**
732

	WT	Mutant
Fgfr2^{C}	553 bp	655 bp
Fgfr2^{PG}	377 bp	611 bp
Fgfr2^{F}	379 bp	614 bp
Fgfr2^{KD}	350 bp After AluI digest	300 bp After AluI digest

733
734

735 **Supplementary information Table S7**

	Source	Identifier
Antibodies		
FGFR2	Abcam	#ab109372
CRKL	Santa Cruz Biotechnology	#sc-319
FRS2	Santa Cruz Biotechnology	#sc-8318
FLAG2-M2	Sigma	#F1804
phospho-p44/42 MAPK Thr202/Tyr204	Cell Signaling Technology	#9101
p44/42 MAPK	Cell Signaling Technology	#9102
GAPDH	ProteinTech	#60004-1-Ig
phospho-AKT Ser473	Cell Signaling Technology	#4060
AKT	Cell Signaling Technology	#9272
phospho-p38	Cell signaling Technology	#4511
p38	Cell signaling Technology	#9212
phospho-PLCγ1 (Y783)	Cell Signaling Technology	#2821
PLCγ1	Cell Signaling Technology	#2822
phospho-JNK	Cell Signaling Technology	#4671
STAT3α	Cell signaling Technology	#8768
phospho-STAT3 (Y705)	Cell Signaling Technology	#9145
phospho-FAK	Cell Signaling Technology	#3283
FAK	Cell Signaling Technology	#3285
Paxillin	Abcam	#ab32084
IRS2	Cell Signaling Technology	#3089
β-catenin	Cell Signaling Technology	#8480
Neurofilament antibody	DSHB	#Clone 2H3
EOMES	Abcam	#ab23345
CDX2	Biogenex	#MU392A-UC
GFP	AvesLab	#GFP-1020
SMA	Cell Signaling Technology	#19245
Peroxidase AffiniPure Goat Anti-Mouse IgG (H+L)	Jackson ImmunoResearch Laboratories	#115-035-003

Peroxidase AffiniPure Goat Anti-Rabbit IgG (H+L)	Jackson ImmunoResearch Laboratories	#111-035-003
Donkey anti-Rabbit IgG (H+L), Alexa Fluor 488	ThermoFisher Scientific	#A-21206
Donkey anti-Rabbit IgG (H+L), Alexa Fluor 546	ThermoFisher Scientific	#A-10040
Donkey anti-Rabbit IgG (H+L), Alexa Fluor 647	ThermoFisher Scientific	#A-31573
Donkey anti-Mouse IgG (H+L), Alexa Fluor 488	ThermoFisher Scientific	#A-21202
Donkey anti- Mouse IgG (H+L), Alexa Fluor 546	ThermoFisher Scientific	#A-10036
Donkey anti- Mouse IgG (H+L), Alexa Fluor 647	ThermoFisher Scientific	#A-31571
Alexa Fluor® 488 AffiniPure Donkey Anti-Chicken IgY (IgG) (H+L)	Jackson ImmunoResearch Laboratories	#703-545-155

736

737 **METHODS**

738 ***Generation of knock-in mice.*** Four distinct targeting vectors carrying the *Fgfr2*^{F}, *Fgfr2*^{C}, *Fgfr2*^{PG},
739 and *Fgfr2*^{KD} mutations were generated. The *Fgfr2*^{F} targeting vector was generated by cloning a
740 short homology arm (1.7kb region between exon 9-10) and a long homology arm (5.1kb, spanning
741 exon10) into PGKneolox2DTA.2 [48]. To allow recombineering into SW105 bacteria, the neo
742 cassette was subsequently replaced by PGKEm7neo flanked by FRT sites, which contains both
743 a eukaryotic and a prokaryotic promoter. Similarly, for the *Fgfr2*^{C} targeting vector, we cloned a
744 long homology arm (5.3kb region spanning exon11) and a short homology arm (1.7kb region
745 between exon 11-12) into PGKneolox2DTA.2 and used a PGKEm7neo flanked by both FRT and
746 LoxP sites for recombineering. For the *Fgfr2*^{PG} targeting vector, we cloned a short homology arm
747 (1.9kb region 5' of exon19) and a long homology arm (5.4kb spanning exon19 and 3'-UTR) into
748 PGKneolox2DTA.2 and used a PGKEm7neo flanked by FRT sites for recombineering. For *Fgfr2*^{KD}
749 targeting vector, we cloned short homology arm (1.9kb SmaI to MfeI, spanning exon 12) and a
750 3.7kb long homology arm (MfeI to BclI, spanning exon 13) into PGKneolox2DTA.2 [48]. Details of
751 regions corresponding to homology arms are provided in Supplementary Information Table S3.

752 For all four alleles, site-directed mutagenesis (SDM) was performed using Phusion
753 polymerase (NEB#M0530). Nucleotide substitutions introduced by SDM in exon10 for *Fgfr2*^{F}
754 allele (introduces an XmaI site), exon11 for *Fgfr2*^{C} allele (introduces a SacI site), exon 19 for
755 *Fgfr2*^{PG} allele (introduces an EcoRI site) and in exon12 for *Fgfr2*^{KD} allele (introduces an AluI site)
756 are provided below. All introduced mutations were verified by sequencing. Details of nucleotide
757 substitutions in *Fgfr2* signaling mutations are provided in Supplementary Information Table S4.

758 The targeting vectors for *Fgfr2*^{F} (linearized with NotI), *Fgfr2*^{C} (linearized with XhoI), *Fgfr2*^{PG}
759 (linearized with NotI) and *Fgfr2*^{KD} (linearized with NotI) were electroporated into 129S4 AK7 ES
760 cells. For generating the allelic series of signaling mutations, ES cells were targeted first with the
761 C targeting vector generating *Fgfr2*$^{+/C}$ mutant cells. After verifying for correct targeting events, the
762 neo cassette was removed by transient transfection with PGKCrebpA, leaving a single LoxP site
763 behind (Figure 3C). *Fgfr2*$^{+/C}$ ES cells were then targeted using the PG targeting vector generating
764 either *Fgfr2*$^{+/PG}$ or *Fgfr2*$^{+/CPG}$ mutant cells, as determined by breeding of the chimeras to
765 *ROSA26*^{Flpo} mice [49]. After verifying for correct targeting events, the neo cassette was removed by
766 transient transfection with PGKFlpobpA [50], leaving both an FRT site and a LoxP site behind
767 (Figure 3C). *Fgfr2*$^{+/CPG}$ neo^{-} ES cells were finally targeted with the F targeting vector, resulting in
768 *Fgfr2*$^{+/F}$ or *Fgfr2*$^{+/FCPG}$ mutant ES cells, as determined by breeding. After verifying for correct
769 targeting events, the neo cassette was removed by transient transfection with Flpe, which is less
770 efficient than Flpo in ES cells [50], in order to not recombine sequences between exons 10-18 due

771 to the retention of the FRT site during the generation of the *Fgfr2*^{PG} allele. We screened targeting
772 events initially by PCR coupled with restriction digestion to identify incorporation of nucleotide
773 substitutions. Proper targeting was confirmed by Southern blotting using 5′ external and 3′
774 external probes amplified using the following primer pairs and then an internal probe against Neo.
775 Primers used to generate probes for confirming targeted clones using Southern blots are
776 described in Supplementary Information Table S5.
777 ES cell chimeras were bred to *Meox2-Cre* or *ROSA26Flpo* deleter mice [49,51] maintained
778 on a 129S4 genetic background to remove the neomycin selection cassette and the deleter alleles
779 were subsequently crossed out. Two independent mouse lines were generated from independent
780 ES cell clones for each allele, and phenotypes were confirmed in both lines. The *Fgfr2*^{C}, *Fgfr2*^{PG},
781 *Fgfr2*^{F}, *Fgfr2*^{FCPG} and *Fgfr2*^{KD} alleles were maintained on the 129S4 genetic background. *Fgfr2*^{C},
782 *Fgfr2*^{PG}, *Fgfr2*^{F} and *Fgfr2*^{KD} mice were genotyped using oligonucleotides listed in Supplementary
783 Information Table S5 and S6, with the F, C or PG primers all being able to genotype *Fgfr2*^{FCPG}
784 mice.

785 ***Mouse strains.*** All animal experimentation was conducted according to protocols approved by
786 the Institutional Animal Care and Use Committee of the Icahn School of Medicine at Mount Sinai.
787 *Fgfr1*$^{cKO/cKO}$, *Fgfr2*$^{cKO/cKO}$, *Fgfr1-GFP* and *Fgfr2-mCherry* were previously described [18,48]. *Fgfr1*
788 signaling mutations [7] are referred to as *Fgfr1*^{C}, *Fgfr1*^{F}, *Fgfr1*^{CPG} and *Fgfr1*^{FCPG}. *Tg(Wnt1-cre)11Rth*,
789 *Tg(Wnt1-cre)2Sor*, *Cdkn2a*$^{+/tm1Rdp}$, *Gt(ROSA)26Sor*$^{tm4(ACTB-tdTomato,-EGFP)Luo}$, and *Bcl2l11*$^{tm1.1Ast}$ are
790 referred to in the text as *Wnt1-Cre*, *Wnt1-Cre2*, *Ink*, *ROSA26*$^{mT/mG}$, and *Bim* respectively [8,9,52-54].
791 All lines were maintained on a 129S4 co-isogenic background, except for *Bim* which was crossed
792 into the *Fgfr1/2* deficient backgrounds after only six generations of backcrossing to 129S4.

793 ***Generation of Fgfr2*$^{-Flag3x}$ *expression vector* and stable 3T3 expression lines.** An *Fgfr2*
794 isoform "c" cDNA isoform was PCR amplified from primary MEFs derived from *Fgfr2*$^{+/+}$, *Fgfr2*$^{PG/PG}$,
795 *Fgfr2*$^{CPG/CPG}$, *Fgfr2*$^{F/F}$ and *Fgfr2*^{FCPGFCPG} and subsequently digested with HindIII and XhoI. The
796 fragments were cloned in the pcDNA expression vector and sequence verified. Linearized
797 pcDNA-FGFR2 plasmids were transfected in 3T3 cells cultured in DMEM supplemented with 10%
798 calf serum (HyClone Laboratories #SH30072.03) with 50U/mL each penicillin and streptomycin
799 (Gibco #P0781). Stable clones were selected in 500μg/mL G418 (Fischer Scientific #BP6735).
800 10 clones from each construct (FGFR2^{wt}-, FGFR2^{PG}-, FGFR2^{CPG}-, FGFR2^{F}-, or FGFR2^{FCPG}-
801 Flag3x) were expanded and assessed for FLAG expression by western blot. Clones expressing
802 high FGFR2-FLAG levels were selected for further analysis.

803 ***Coimmunoprecipitation and Western blotting.*** Stable 3T3 cells expressing $FGFR2^{WT}$,
804 $FGFR2^{PG}$, $FGFR2^{CPG}$, $FGFR2^{F}$, or $FGFR2^{FCPG}$ -Flag3x were serum-starved (0.1% calf serum
805 supplemented DMEM) overnight, stimulated for 15 mins with 50 ng/mL FGF1 (PeproTech, 450-
806 33A) or FGF8b (PeproTech 100-25B) and 5 µg/mL heparin (Sigma #H3149), and lysed in ice-
807 cold NP-40 lysis buffer (20 mM Tris HCL at pH 8, 137 mM NaCl, 10% glycerol, 1% Nonidet [NP-
808 40], 2 mM EDTA, 25 mM β glycerol phosphate, 1 mM Na_3VO_4, 10 mM NaF, 1× cOmplete, EDTA-
809 free Protease Inhibitor Cocktail. 800 µg cell lysates were subsequently used for
810 immunoprecipitation with Anti-FLAG M2 magnetic beads (Sigma #M8823) using the
811 manufacturer's protocol. We incubated lysates with anti-FLAG M2 magnetic beads overnight at
812 4°C followed by five washes with lysis buffer, and precipitated proteins were eluted in Laemmli
813 buffer (10% glycerol, 2% SDS, 0.002% bromophenol blue, 0.062M Tris-HCl, pH 6.8) containing
814 10% β-mercaptoethanol, heated for 5 min at 95°C, separated by SDS-PAGE and analyzed by
815 western blots.
816 Western blot analysis was performed according to standard protocols using horseradish
817 peroxidase-conjugated secondary antibodies (1:10,000 dilution) developed by chemiluminescent
818 HRP substrate. Primary antibodies were used at the following dilutions for Western blotting:
819 FGFR2 (1:500 dilution), CRKL (1:500 dilution), FRS2 (1:500 dilution), Flag2 M2 (1:500 dilution),
820 phospho-p44/42 MAPK (1:1,000 dilution), p44/42 MAPK (1:1,000 dilution), GAPDH (1:1000
821 dilution), phospho-AKT (1:1,000 dilution), AKT (1:1,000 dilution), phospho-p38 (1:500 dilution),
822 p38 (1:500 dilution), phospho-PLCγ1 (Y783) (1:200 dilution), PLCγ1 (1:1000 dilution), pJNK
823 (1:500 dilution), phospho-STAT3 (Y705) (1:500 dilution), STAT3α (1:1000 dilution), phospho-FAK
824 (1:1000 dilution), FAK (1:1000 dilution), β-catenin (1:1000 dilution), Paxillin (1:1000 dilution), and
825 IRS2 (Cell Signaling Technology, 3089). For signaling pathways analyzed, the blots were
826 quantified for three independent biological replicates using ImageLab6.0 analysis tool. Ratio of
827 average of mean intensity value of pERK1/2, pAKT, pPLCγ1, pJNK, pSTAT3α, pP38 to GAPDH
828 ± standard deviation was plotted for each pathway.
829
830 ***Cell derivation and culture conditions.*** Primary iFNPs were generated by dissecting the
831 maxillary and nasal prominences of E11.5 *Fgfr2*$^{+/+}$*; Ink*$^{-/-}$, *Fgfr2*$^{F/F}$*; Ink*$^{-/-}$, *Fgfr2*$^{CPG/CPG}$*; Ink*$^{-/-}$, and
832 E9.5 or E11.5 *Fgfr2*$^{FCPG/FCPG}$*; Ink*$^{-/-}$ embryos in PBS. The tissue was disassociated with 0.125%
833 Trypsin-EDTA and cultured in DMEM supplemented with 20% FBS, 50 U/mL each penicillin and
834 streptomycin on fibronectin coated plates (0.5µg/cm^2). Cells were subsequently split 1:5 through
835 for at least 5 passages before immortalized cell lines were obtained. Cells were allowed to grow
836 until sub-confluent. All experiments were performed between passage 15 and 25. We used PX459

837 V2.0 vector (Addgene plasmid # 62988) to CRISPR out either *Fgfr1* or *Fgfr2* and create *Fgfr1* null,
838 *Fgfr2* null, or *Fgfr1*: *Fgfr2* double null cells. gRNA sequences for *Fgfr1* and *Fgfr2* were selected
839 using CHOPCHOP gRNA design web tool and were cloned using the oligonucleotides
840 (Supplementary Information Table S5), as previously described [55]. Plasmids were transfected in
841 respective iFNP cells cultured in DMEM (Sigma #5796) supplemented with 10% calf serum with
842 50 U/mL each penicillin and streptomycin. Stable clones were selected in 5μg/mL Puromycin
843 (Sigma #P8833). Clones were verified (homozygous deletion of exon6 for *Fgfr1* and deletion
844 exon5 for *Fgfr2* which also introduces a frameshift mutation) using PCR (Supplementary
845 Information Table S5). Primary MEFs were derived from E12.5 wild type mice embryos. Embryos
846 were eviscerated and after removing the head, remaining tissue was chopped into 1 cm pieces
847 and incubated in (0.25%) 1 mL trypsin-EDTA (ThermoFisher # 25200-072) for 30 mins with
848 intermittent shaking. 10 mL DMEM 10% calf serum was added and the mixture was allowed to
849 pass through a cell-strainer. Cells collected from each embryo was plated in 0.2% gelatin
850 (Sigma #G1393) coated 15cm plate.

851 ***Skeletal preparations.*** Embryos at E14.5, E16.5 or E18.5 embryos were skinned, eviscerated,
852 fixed in 95% ethanol overnight, and stained (0.015% Alcian blue, 0.005% Alizarin red, 5% glacial
853 acetic acid, in 70% ethanol) overnight at 37°C. Skeletons were then cleared in 1% KOH and
854 transferred to decreasing concentrations of KOH in increasing concentrations of glycerol until
855 clear.

856 ***Acetocarmine and hematoxylin and eosin staining.*** Freshly harvested tissue was fixed in 4%
857 PFA at 4°C overnight followed by dehydration in 70% ethanol. For acetocarmine staining, tissues
858 were incubated in 0.5% aceto-carmine (0.5 g carmine stain (Sigma #C1022) dissolved in 100 ml
859 boiling 45% acetic acid for 15 minutes), followed by de-staining in 70% ethanol for 1 minute and
860 1% acid alcohol (1% HCl in 70% ethanol) for 2 minutes and 5% acid alcohol (5% HCl in 70%
861 ethanol) for 1 minute. For hematoxylin and eosin staining, freshly harvested tissues were
862 dissected in PBS, and fixed in 4% PFA followed by dehydration through a graded ethanol series,
863 and embedded in paraffin. 5μm sections were cut. After deparaffinization and rehydration,
864 sections were stained with Harris modified hematoxylin (Sigma #HHS16) followed by a 10 second
865 wash in acid-alcohol (1% v/v HCl in 70% EtOH), followed by counterstaining with 1% eosinY
866 (Sigma #17372-87-1). Tissues were washed and mounted with Permount (ThermoFisher
867 Scientific #SP15100).

868 ***Scratch assays.*** Cells were seeded onto glass coverslips coated with 5 µg/mL human plasma
869 fibronectin purified protein (Millipore Sigma #FC010). At ~90–100% confluency, cells were
870 scratched with a P1000 pipet tip, washed with PBS and incubated in fresh medium containing
871 either 0.1% FBS, 10% FBS, 50 ng/mL FGF1 and 5 µg/mL heparin or 10 ng/mL PDGF-AA (R&D
872 Systems #1055-AA-050) supplemented DMEM for 12 hrs.

873 ***Immunofluorescence and Antibodies.*** For immunostaining whole mount embryos were fixed in
874 4% paraformaldehyde solution (PFA) in PBS overnight and washed with PBS five times,
875 permeabilized with 0.5% Triton X100 in PBS for 30 min and blocked in 2% blocking serum for 2h
876 at room temperature. Primary anti-neurofilament antibody (Clone 2H3, DSHB) was used at a 1:20
877 dilution in 1% donkey serum in PBST; embryos were incubated overnight at 4°C. The next day,
878 embryos were washed 4 times in PBST and incubated with anti-mouse HRP-conjugated
879 secondary antibodies at a 1:1000 dilution for 4hrs at room temperature followed by washing in
880 PBST 4 times and signal was developed using ImmPACTDAB kit (VectorLabs #SK-4105). For
881 whole-mount immunofluorescence at E7.5, embryos were fixed overnight in 4:1 methanol:DMSO.
882 Primary antibodies for Eomes (1:100 dilution) and Cdx2 (1:100 dilution) were used. For
883 immunostaining cells, cells were fixed for 10 mins in 4% PFA in PBS at room temperature. Cells/
884 tissues were subsequently processed for immunofluorescence analysis as detailed above using
885 anti-paxillin primary antibody (1:250 dilution) with Alexa647 conjugated phalloidin (1:40 dilution).
886 For immunofluorescence on sections, antibodies for GFP (1:100 dilution), mCherry (1:100 dilution)
887 and SMA (1:100 dilution) was used. Supplementary Information Table S7 provides more
888 information on antibodies used in this study. Embryos were stained with DAPI following fixation
889 as previously described [56]. Cells / tissues were photographed using an Olympus DP71 digital
890 camera fitted onto an Olympus BX51 fluorescence microscope, Leica SP5 confocal or a
891 Hamamatsu C11440 camera fitted to a Zeiss Observer Z1 microscope. Epifluorescence was
892 imaged in Zeiss Axioplan fitted to ProgRes CT3 camera.

893 ***In situ hybridization.*** Labeled antisense-RNA probes were synthesized for *Alx3, Msx1, Six3,*
894 *Nkx2.1, Fgf8, Shh, Col2a1, Col10a1* and *Meox1*. Digoxigenin-labeled anti-sense probes were
895 generated as described, and mRNA in situ hybridization on paraffin sections for chromogenic
896 detection was performed using standard protocols.

897 ***Micro-CT imaging.*** Micro-CT imaging of the skulls were performed using a SkyScan 1172
898 scanner (Bruker, Kontich, Belgium). The mouse heads were dissected and fixed in 10% neutral
899 buffered formalin and washed and stored in PBS at 4 °C. The skull bones were scanned with

900 settings of 50 kV, 500 µA, 10 µm pixel resolution, 0.3° rotation steps, and 4 frames average
901 imaging with a 0.5-mm Al filter at Micro-CT Core, School of Dentistry, NYU, New York. The
902 acquired X-ray projections were reconstructed using the Imaris software (Oxford Instruments).

903 ***Cell proliferation assay.*** For EdU labeling in mice, pregnant females were injected
904 intraperitoneally with 100 mg/kg body weight of EdU. EdU detection was carried out as per
905 manufacturer's instruction for Click-iT EdU Cell Proliferation Kit.

906 ***TUNEL assay.*** Sections were deparaffinized and were rehydrated in PBS, followed by post-
907 fixation in 4% PFA. In Situ Cell Death Detection Kit, TMR red user protocol was used to detect
908 cell death.

909 ***RT-qPCR.*** Cells were lysed, and mRNA was extracted according to Qiagen RNeasy kit standard
910 protocol. cDNA was synthesized using a 2:1 ratio of random primers to Oligo(dT) with SuperScript
911 IV RT (Invitrogen). qPCR was performed with PerfeCTa SYBR Green FastMix for iQ (Quanta
912 Biosciences) with Bio-Rad iQ5 multicolor real-time PCR detection system and analyzed with Bio-
913 Rad iQ5 optical system software (version 2.0). Cycling conditions were as follows: step 1, 3 min
914 at 95°C; step 2, 10 sec at 95°C; step 3, 30 sec at 60°C; and repeat steps 2 and 3 for 40 cycles.
915 Proper amplification was confirmed using a melting curve and by running samples on a gel to
916 ensure that the correct size band was obtained. Graphs were made using Microsoft Excel and
917 Prism. Primer sequence for respective genes used for RT-qPCR analysis is listed below.

918 **β-Catenin Quantification.** Cells were stained and imaged using a Leica SP5 confocal
919 microscope under identical conditions. Stacks were then background subtracted using a 100px
920 rolling ball function in ImageJ. The average pixel intensity along cell-cell junctions was measured
921 in a single z-plane per junction using a 15-pixel line width in ImageJ for the EGFP and β-catenin
922 channels.

923 **Quantification and statistical analysis.** Statistical analysis was performed using GraphPad
924 Prism6.0 and Microsoft Excel. Values are presented as mean ± standard deviation. The statistical
925 significance was determined using a student *t*-test with Holm-Sidak method.

926

927 **References**

928

929 1 Lemmon, M. A. & Schlessinger, J. Cell signaling by receptor tyrosine kinases. *Cell* **141**,
930 1117-1134, doi:10.1016/j.cell.2010.06.011 (2010).
931 2 Zinkle, A. & Mohammadi, M. A threshold model for receptor tyrosine kinase signaling
932 specificity and cell fate determination. *F1000Res* **7**, doi:10.12688/f1000research.14143.1
933 (2018).
934 3 Li, P. & Elowitz, M. B. Communication codes in developmental signaling pathways.
935 *Development* **146**, doi:10.1242/dev.170977 (2019).
936 4 Vasudevan, H. N., Mazot, P., He, F. & Soriano, P. Receptor tyrosine kinases modulate
937 distinct transcriptional programs by differential usage of intracellular pathways. *Elife* **4**,
938 doi:10.7554/eLife.07186 (2015).
939 5 Brewer, J. R., Mazot, P. & Soriano, P. Genetic insights into the mechanisms of Fgf signaling.
940 *Genes Dev* **30**, 751-771, doi:10.1101/gad.277137.115 (2016).
941 6 Lanner, F. & Rossant, J. The role of FGF/Erk signaling in pluripotent cells. *Development*
942 **137**, 3351-3360 (2010).
943 7 Brewer, J. R., Molotkov, A., Mazot, P., Hoch, R. V. & Soriano, P. Fgfr1 regulates
944 development through the combinatorial use of signaling proteins. *Genes Dev* **29**, 1863-
945 1874, doi:10.1101/gad.264994.115 (2015).
946 8 Danielian, P. S., Muccino, D., Rowitch, D. H., Michael, S. K. & McMahon, A. P. Modification
947 of gene activity in mouse embryos in utero by a tamoxifen-inducible form of Cre
948 recombinase. *Curr Biol* **8**, 1323-1326, doi:10.1016/s0960-9822(07)00562-3 (1998).
949 9 Lewis, A. E., Vasudevan, H. N., O'Neill, A. K., Soriano, P. & Bush, J. O. The widely used
950 Wnt1-Cre transgene causes developmental phenotypes by ectopic activation of Wnt
951 signaling. *Dev Biol* **379**, 229-234, doi:10.1016/j.ydbio.2013.04.026 (2013).
952 10 Partanen, J., Schwartz, L. & Rossant, J. Opposite phenotypes of hypomorphic and Y766
953 phosphorylation site mutations reveal a function for Fgfr1 in anteroposterior patterning
954 of mouse embryos. *Genes Dev* **12**, 2332-2344 (1998).
955 11 De Moerlooze, L. *et al.* An important role for the IIIb isoform of fibroblast growth factor
956 receptor 2 (FGFR2) in mesenchymal-epithelial signalling during mouse organogenesis.
957 *Development* **127**, 483-492 (2000).
958 12 Youle, R. J. & Strasser, A. The BCL-2 protein family: opposing activities that mediate cell
959 death. *Nat Rev Mol Cell Biol* **9**, 47-59, doi:10.1038/nrm2308 (2008).
960 13 Chipuk, J. E. & Green, D. R. How do BCL-2 proteins induce mitochondrial outer membrane
961 permeabilization? *Trends Cell Biol* **18**, 157-164, doi:10.1016/j.tcb.2008.01.007 (2008).
962 14 Czabotar, P. E., Lessene, G., Strasser, A. & Adams, J. M. Control of apoptosis by the BCL-2
963 protein family: implications for physiology and therapy. *Nat Rev Mol Cell Biol* **15**, 49-63,
964 doi:10.1038/nrm3722 (2014).
965 15 Grabow, S. *et al.* Subtle Changes in the Levels of BCL-2 Proteins Cause Severe Craniofacial
966 Abnormalities. *Cell Rep* **24**, 3285-3295 e3284, doi:10.1016/j.celrep.2018.08.048 (2018).
967 16 Clybouw, C. *et al.* Alternative splicing of Bim and Erk-mediated Bim(EL) phosphorylation
968 are dispensable for hematopoietic homeostasis in vivo. *Cell Death Differ* **19**, 1060-1068,
969 doi:10.1038/cdd.2011.198 (2012).

970 17 Lei, K. & Davis, R. J. JNK phosphorylation of Bim-related members of the Bcl2 family
971 induces Bax-dependent apoptosis. *Proc Natl Acad Sci U S A* **100**, 2432-2437,
972 doi:10.1073/pnas.0438011100 (2003).
973 18 Molotkov, A., Mazot, P., Brewer, J. R., Cinalli, R. M. & Soriano, P. Distinct Requirements
974 for Fgfr1 and Fgfr2 in Primitive Endoderm Development and Exit from Pluripotency.
975 *Developmental Cell* **41**, 511-526 (2017).
976 19 Yu, K. *et al.* Conditional inactivation of FGF receptor 2 reveals an essential role for FGF
977 signaling in the regulation of osteoblast function and bone growth. *Development* **130**,
978 3063-3074 (2003).
979 20 Xu, X. *et al.* Fibroblast growth factor receptor 2 (FGFR2)-mediated reciprocal regulation
980 loop between FGF8 and FGF10 is essential for limb induction. *Development* **125**, 753-765
981 (1998).
982 21 Garg, A. *et al.* Alx4 relays sequential FGF signaling to induce lacrimal gland morphogenesis.
983 *PLoS Genet* **13**, e1007047, doi:10.1371/journal.pgen.1007047 (2017).
984 22 Steinberg, Z. *et al.* FGFR2b signaling regulates ex vivo submandibular gland epithelial cell
985 proliferation and branching morphogenesis. *Development* **132**, 1223-1234,
986 doi:10.1242/dev.01690 (2005).
987 23 Francavilla, C. *et al.* Functional proteomics defines the molecular switch underlying FGF
988 receptor trafficking and cellular outputs. *Mol Cell* **51**, 707-722,
989 doi:10.1016/j.molcel.2013.08.002 (2013).
990 24 Kurowski, A., Molotkov, A. & Soriano, P. FGFR1 regulates trophectoderm development
991 and facilitates blastocyst implantation. *Dev Biol* **446**, 94-101,
992 doi:10.1016/j.ydbio.2018.12.008 (2019).
993 25 Fantauzzo, K. A. & Soriano , P. Generation of an Immortalized Mouse Embryonic Palatal
994 Mesenchyme Cell Line. *PLoS ONE* **12**, e0179078 (2017).
995 26 Hanks, S. K., Quinn, A. M. & Hunter, T. The protein kinase family: conserved features and
996 deduced phylogeny of the catalytic domains. *Science* **241**, 42-52,
997 doi:10.1126/science.3291115 (1988).
998 27 Bellot, F. *et al.* Ligand-induced transphosphorylation between different FGF receptors.
999 *EMBO J* **10**, 2849-2854 (1991).
1000 28 Ueno, H., Gunn, M., Dell, K., Tseng, A., Jr. & Williams, L. A truncated form of fibroblast
1001 growth factor receptor 1 inhibits signal transduction by multiple types of fibroblast
1002 growth factor receptor. *J Biol Chem* **267**, 1470-1476 (1992).
1003 29 Meyer, M. *et al.* FGF receptors 1 and 2 are key regulators of keratinocyte migration in
1004 vitro and in wounded skin. *J Cell Sci* **125**, 5690-5701, doi:10.1242/jcs.108167 (2012).
1005 30 Rasouli, S. J. *et al.* The flow responsive transcription factor Klf2 is required for myocardial
1006 wall integrity by modulating Fgf signaling. *Elife* **7**, doi:10.7554/eLife.38889 (2018).
1007 31 Sun, J. & Stathopoulos, A. FGF controls epithelial-mesenchymal transitions during
1008 gastrulation by regulating cell division and apicobasal polarity. *Development* **145**,
1009 doi:10.1242/dev.161927 (2018).
1010 32 Yayon, A., Klagsbrun, M., Esko, J. D., Leder, P. & Ornitz, D. M. Cell surface, heparin-like
1011 molecules are required for binding of basic fibroblast growth factor to its high affinity
1012 receptor. *Cell* **64**, 841-848, doi:10.1016/0092-8674(91)90512-w (1991).

1013 33 Rapraeger, A. C., Krufka, A. & Olwin, B. B. Requirement of heparan sulfate for bFGF-
1014 mediated fibroblast growth and myoblast differentiation. *Science* **252**, 1705-1708,
1015 doi:10.1126/science.1646484 (1991).
1016 34 Endo, Y., Ishiwata-Endo, H. & Yamada, K. M. Extracellular matrix protein anosmin
1017 promotes neural crest formation and regulates FGF, BMP, and WNT activities. *Dev Cell* **23**,
1018 305-316, doi:10.1016/j.devcel.2012.07.006 (2012).
1019 35 Geiger, B. & Yamada, K. M. Molecular architecture and function of matrix adhesions. *Cold*
1020 *Spring Harb Perspect Biol* **3**, doi:10.1101/cshperspect.a005033 (2011).
1021 36 McQuade, K. J., Beauvais, D. M., Burbach, B. J. & Rapraeger, A. C. Syndecan-1 regulates
1022 alphavbeta5 integrin activity in B82L fibroblasts. *J Cell Sci* **119**, 2445-2456,
1023 doi:10.1242/jcs.02970 (2006).
1024 37 Moser, M., Legate, K. R., Zent, R. & Fassler, R. The tail of integrins, talin, and kindlins.
1025 *Science* **324**, 895-899, doi:10.1126/science.1163865 (2009).
1026 38 Frisch, S. M. & Francis, H. Disruption of epithelial cell-matrix interactions induces
1027 apoptosis. *J Cell Biol* **124**, 619-626, doi:10.1083/jcb.124.4.619 (1994).
1028 39 Mailleux, A. A. *et al.* BIM regulates apoptosis during mammary ductal morphogenesis, and
1029 its absence reveals alternative cell death mechanisms. *Dev Cell* **12**, 221-234,
1030 doi:10.1016/j.devcel.2006.12.003 (2007).
1031 40 Borges, E., Jan, Y. & Ruoslahti, E. Platelet-derived growth factor receptor beta and
1032 vascular endothelial growth factor receptor 2 bind to the beta 3 integrin through its
1033 extracellular domain. *J Biol Chem* **275**, 39867-39873, doi:10.1074/jbc.M007040200
1034 (2000).
1035 41 Klinghoffer, R. A., Hamilton, T. G., Hoch, R. & Soriano, P. An allelic series at the
1036 PDGFalphaR locus indicates unequal contributions of distinct signaling pathways during
1037 development. *Dev Cell* **2**, 103-113 (2002).
1038 42 Tallquist, M. D., French, W. J. & Soriano, P. Additive effects of PDGF receptor beta
1039 signaling pathways in vascular smooth muscle cell development. *PLoS Biol* **1**, E52,
1040 doi:10.1371/journal.pbio.0000052 (2003).
1041 43 Kon, E. *et al.* N-cadherin-regulated FGFR ubiquitination and degradation control
1042 mammalian neocortical projection neuron migration. *Elife* **8**, doi:10.7554/eLife.47673
1043 (2019).
1044 44 Scarpa, E. *et al.* Cadherin Switch during EMT in Neural Crest Cells Leads to Contact
1045 Inhibition of Locomotion via Repolarization of Forces. *Dev Cell* **34**, 421-434,
1046 doi:10.1016/j.devcel.2015.06.012 (2015).
1047 45 Ciruna, B. & Rossant, J. FGF signaling regulates mesoderm cell fate specification and
1048 morphogenetic movement at the primitive streak. *Dev Cell* **1**, 37-49 (2001).
1049 46 Sun, X., Meyers, E. N., Lewandoski, M. & Martin, G. R. Targeted disruption of Fgf8 causes
1050 failure of cell migration in the gastrulating mouse embryo. *Genes Dev* **13**, 1834-1846,
1051 doi:10.1101/gad.13.14.1834 (1999).
1052 47 Nieto, M. A., Huang, R. Y., Jackson, R. A. & Thiery, J. P. Emt: 2016. *Cell* **166**, 21-45,
1053 doi:10.1016/j.cell.2016.06.028 (2016).
1054 48 Hoch, R. V. & Soriano, P. Context-specific requirements for Fgfr1 signaling through Frs2
1055 and Frs3 during mouse development. *Development* **133**, 663-673, doi:10.1242/dev.02242
1056 (2006).

1057 49 Raymond, C. S. & Soriano, P. ROSA26Flpo deleter mice promote efficient inversion of
1058 conditional gene traps in vivo. *Genesis* **48**, 603-606, doi:10.1002/dvg.20659 (2010).
1059 50 Raymond, C. S. & Soriano, P. High-efficiency FLP and PhiC31 site-specific recombination
1060 in mammalian cells. *PLoS One* **2**, e162, doi:10.1371/journal.pone.0000162 (2007).
1061 51 Tallquist, M. D. & Soriano, P. Epiblast-restricted Cre expression in MORE mice: a tool to
1062 distinguish embryonic vs. extra-embryonic gene function. *Genesis* **26**, 113-115 (2000).
1063 52 Bouillet, P. *et al.* Proapoptotic Bcl-2 relative Bim required for certain apoptotic responses,
1064 leukocyte homeostasis, and to preclude autoimmunity. *Science* **286**, 1735-1738,
1065 doi:10.1126/science.286.5445.1735 (1999).
1066 53 Muzumdar, M. D., Tasic, B., Miyamichi, K., Li, L. & Luo, L. A global double-fluorescent Cre
1067 reporter mouse. *Genesis* **45**, 593-605, doi:10.1002/dvg.20335 (2007).
1068 54 Serrano, M. *et al.* Role of the INK4a locus in tumor suppression and cell mortality. *Cell* **85**,
1069 27-37, doi:10.1016/s0092-8674(00)81079-x (1996).
1070 55 Ran, F. A. *et al.* Genome engineering using the CRISPR-Cas9 system. *Nat Protoc* **8**, 2281-
1071 2308, doi:10.1038/nprot.2013.143 (2013).
1072 56 Sandell, L. L., Kurosaka, H. & Trainor, P. A. Whole mount nuclear fluorescent imaging:
1073 convenient documentation of embryo morphology. *Genesis* **50**, 844-850,
1074 doi:10.1002/dvg.22344 (2012).
1075